



HAL
open science

Multiple tectonic-magmatic Mo-enrichment events in Yuleken porphyry Cu-Mo deposit, NW China and its' implications for the formation of giant porphyry Mo deposit

Tao Hong, David Dolejš, Ming-Guo Zhai, Oscar Laurent, Xing-Wang Xu, Jun Gao, Kateřina Schlögllová, Yue-Jun Wang

► To cite this version:

Tao Hong, David Dolejš, Ming-Guo Zhai, Oscar Laurent, Xing-Wang Xu, et al.. Multiple tectonic-magmatic Mo-enrichment events in Yuleken porphyry Cu-Mo deposit, NW China and its' implications for the formation of giant porphyry Mo deposit. *Ore Geology Reviews*, 2021, 139 (Part A), pp.104401. 10.1016/j.oregeorev.2021.104401 . hal-03436645

HAL Id: hal-03436645

<https://hal.science/hal-03436645>

Submitted on 21 Nov 2022

HAL is a multi-disciplinary open access archive for the deposit and dissemination of scientific research documents, whether they are published or not. The documents may come from teaching and research institutions in France or abroad, or from public or private research centers.

L'archive ouverte pluridisciplinaire **HAL**, est destinée au dépôt et à la diffusion de documents scientifiques de niveau recherche, publiés ou non, émanant des établissements d'enseignement et de recherche français ou étrangers, des laboratoires publics ou privés.

Multiple tectonic-magmatic Mo-enrichment events in Yuleken porphyry Cu-Mo deposit, NW China and its' implications for the formation of giant porphyry Mo deposit

Tao Hong^{a,b,c,d}, David Dolejš^d, Ming-Guo Zhai^{c,e,f}, Oscar Laurent^{g,h}, Xing-Wang Xu^{c,f,i}, Jun Gao^{c,f,i}, Kateřina Schlögllová^d, Yue-Jun Wang^{a,b}

^aGuangdong Provincial Key Lab of Geodynamics and Geohazards, School of Earth Sciences and Engineering, Sun Yat-sen University, Guangzhou 510275, China

^bSouthern Marine Science and Engineering Guangdong Laboratory (Zhuhai), Zhuhai 519082, China

^cKey Laboratory of Mineral Resources, Institute of Geology and Geophysics, University of Chinese Academy of Sciences, Beijing 100029, PR China

^dInstitute of Earth and Environmental Sciences, University of Freiburg, 79104 Freiburg i.Br, Germany

^eKey Laboratory of Computational Earth Dynamics, College of Earth and Planetary Sciences, University of Chinese Academy of Sciences, Beijing 100049, China

^fInnovation Academy for Earth Sciences, CAS, Beijing 100029, PR China

^gInstitute for Geochemistry and Petrology, ETH Zürich, Zürich CH-8092, Switzerland

^hGéosciences Environnement Toulouse – Observatoire Midi-Pyrénées, Toulouse 31400, France

ⁱUniversity of Chinese Academy of Sciences, Beijing 100049, PR China

Abstract

The Yuleken porphyry Cu-Mo deposit located in the Chinese Altay-East Junggar, a section of the Central Asian Orogenic Belt, the world's largest Phanerozoic subduction-accretionary orogen, witnessed the multistage tectonic-magmatic evolution and mineralization from arc to syn- and post-collision environment over a time span of about 52 Ma. Four types of molybdenite have been distinguished: (1) primary magmatic-hydrothermal, undeformed molybdenite in porphyry, (2) recrystallized molybdenite associated with ductile deformation, (3) recrystallized, intrafoliation molybdenite, and (4) fracture-related hydrothermal molybdenite, and these are characterized by decreasing Re abundances from magmatic to hydrothermal conditions. Individual molybdenite types are non-stoichiometric and exhibit the following negative correlation between the Mo and Re contents:

$$\text{Re (apfu)} = -0.0026 \text{ Mo (apfu)} + 0.00268.$$

This trend reflects successive stages of tectonic-hydrothermal events from a magmatic island-arc to a post-collisional setting. These repetitive mineralization events produced Mo enrichment and higher overall Mo grade of the Yuleken deposit, and are recorded in progressively decreasing Re concentrations in molybdenite. Statistical evaluation of Mo and Re abundances in giant to small porphyry deposits worldwide also indicates that decreasing Re in molybdenite will lead to lower overall Re resource (in a single deposit) and to greater overall Mo resource (in the same deposit). Multiple mineralization processes related to repetitive tectonomagmatic episodes in large porphyry Mo deposits that display Re depletion in molybdenite suggest that reworking of mantle-derived porphyry systems by successive events of crustal growth may be the responsible for Mo enrichment and higher overall Mo ore grade, and eventually produce giant porphyry molybdenum deposits.

Keywords

Porphyry deposits, Re-Mo, Molybdenite, Trace elements, Multiple Mo enrichment

1. Introduction

The majority of the world's molybdenum resources is derived from porphyry Mo and Cu-Mo deposits. Giant (Mo reserve > 0.5 Mt) and large (Mo reserve of 0.1–0.5 Mt) porphyry Mo deposits with low concentrations of Re supply nearly 60 % of the global Mo demand (Chen et al., 2017a, Chen et al., 2017b, Chen et al., 2017c, Gao et al., 2018). Porphyry Cu-Mo deposits with high concentrations of Re are also its primary source (Sinclair et al., 2016). Re is almost invariably concentrated in molybdenite because the ionic radius of Re⁴⁺ is very close to that of Mo⁴⁺ and it allows the substitution of Re for Mo in molybdenite (Morris and Short, 1969, Shannon, 1976, Sinclair et al., 2016). Large to giant porphyry Mo deposits, which formed in continental collision orogens or in intracrustal rifts through partial melting of Precambrian crust (Chen et al., 2017a, Gao et al., 2018) usually have low Re concentrations in molybdenite (Sinclair et al., 2016), whereas porphyry Cu-Mo deposits formed in ocean island arcs typically have small Mo reserves but high-Re molybdenite (Audétat, 2010, Zhu et al., 2010, Richards, 2011). As accretion of island arcs is one mechanism for the formation of continental crust (Suyehiro et al., 1996), porphyry Mo deposits that formed in the continental crust could potentially be derived from the remnant arcs. The role of molybdenum formed in ocean island arcs, pre-enrichment in porphyry Cu-Mo deposits and the origin of giant porphyry Mo deposits found in late to post-collisional continental tectonic settings are therefore poorly understood.

Most giant porphyry Mo deposits have undergone multiple tectonic and magmatic events (Li et al., 2014, Mi et al., 2015, Li and Pirajno, 2017), and the relationship between tectonic-magmatic events and the formation of low Re molybdenite is also critical for the understanding of the formation of porphyry deposits. Textural and compositional variations in molybdenite are well preserved in porphyry Cu-Mo deposits in the Central Asian Orogenic Belt (CAOB; Xue et al., 2016, Gao et al., 2018) and can be used to decipher the key factors affecting the Re content of molybdenite.

The Yuleken (also called Yulekenhalasu) porphyry Cu-Mo deposit (PCMD) in China is one of several subduction-related deposits in the Kalaxian'gar porphyry copper belt (KPCB), in the central part of the Central Asian metallogenic domain (CAMD; [Gao et al., 2018](#), [Wu et al., 2019](#)). The Yuleken deposit preserves evidence of syn- to post-collisional metallogenic overprint ([Hong et al., 2015](#), [Xue et al., 2016](#), [Hong et al., 2018a](#), [Hong et al., 2018b](#)), making it a unique target to investigate the behavior and evolution of molybdenite induced by superimposed [mineralization](#) events. We report textural and compositional of molybdenite from different ore-forming stages in order to investigate: (1) the Re and Mo variation in molybdenite during superimposed ore-forming processes, (2) if the Re variation in molybdenite can be used as an indicator of multiple mineralization stages, and (3) the Re contents in a wide spectrum of Re-Mo deposits and their global implications.

2. Geological setting

2.1. Regional geology

The Yuleken PCMD is located about 40 km southwest of Qinghe City, China, at the northern margin of the Junggar [Terrane](#) ([Fig. 1a](#)). This deposit is located within the Saur Devonian–Carboniferous oceanic [island arc](#) and incorporated at the late Paleozoic [continental margin](#) of the Kazakhstan–Junggar Plate ([Glorie et al., 2011](#), [Yang et al., 2014](#), [Xu et al., 2015](#)).

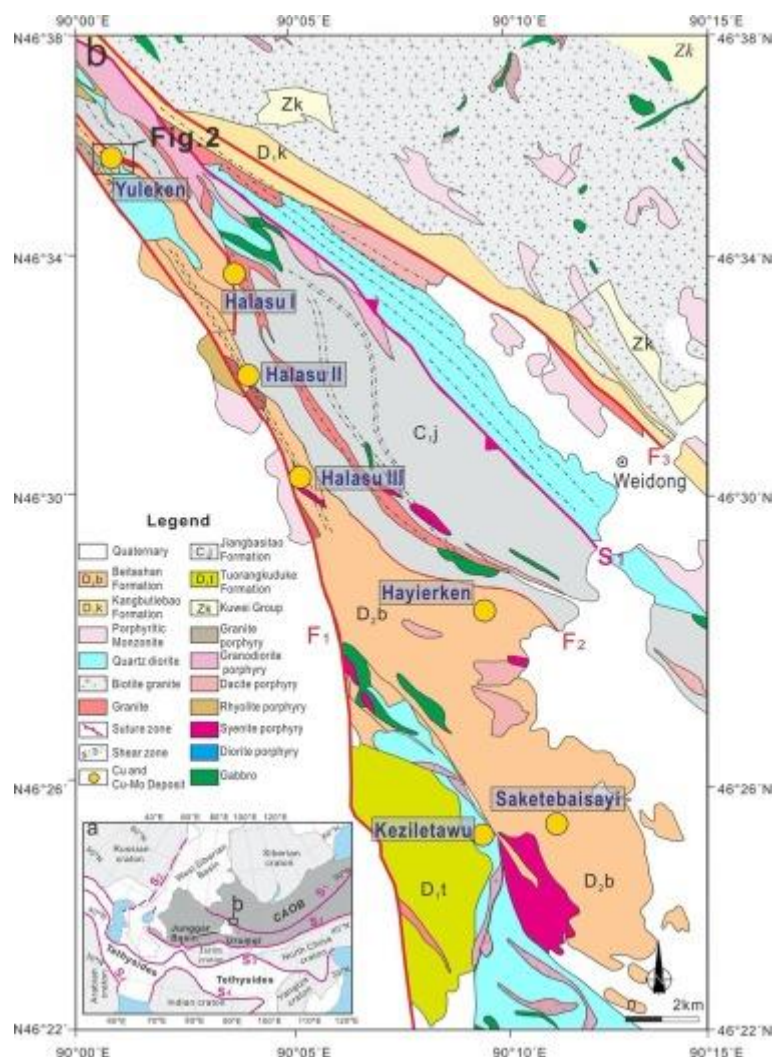


Fig. 1. Geological situation in the Central Asian metallogenic domain (modified after [Xu et al., 2015](#), [Gao et al., 2018](#), [Hong et al., 2018a](#), [Hong et al., 2018b](#)): (a) principal tectonic units and (b) regional geologic map of northern Junggar [terrane](#), northern Xinjiang. Abbreviations: F₁ – Kalaxiang'e'er-Jieledikalatawu fault; F₂ – Yulekenhalasu-Zhuolesay fault; F₃ – Mayinebo fault; S₁ – Zaysan-Irtysh-the Main Mongolian Lineament-Okhotsk suture; S₂ – Ural-Kazakhstan-Tianshan-Solonker suture; S₃ – Kunlun-Altyn-Qilian-Qinling-Dabie suture; S₄ – Alpine-Himalayan suture.

The major [lithologies](#) in the Yuleken area consist of the [Middle Ordovician](#) Habahe Group, the Lower [Devonian](#) Tuorangkuduke Formation, the [Middle Devonian](#) Beitashan Formation, and the Lower Carboniferous Jiangbasitao Formation ([Fig. 1b](#)). The Middle Ordovician Habahe Group is mainly composed of turbiditic and pyroclastic sequences deposited on an active continental margin ([Sun et al., 2008](#), [Long et al., 2010](#)), whereas the Tuorangkuduke Formation is comprised of pyroclastic rocks interbedded with small amounts of terrigenous clastic sedimentary rocks. The Beitashan Formation is composed of mafic to intermediate volcanic

and pyroclastic rocks, with the latter intercalated with minor ultramafic and picritic volcanic rocks and carbonates (Zhang et al., 2008). The Jiangbasitao Formation consists of felsic pyroclastic rocks intercalated with sedimentary rocks having minor pyroclastic components (Yang et al., 2014).

The Beitashan and Jiangbasitao Formations were intruded by Late to Middle Devonian and early Permian silicic magmas, in a subduction-zone to post-collisional environment (Yang et al., 2014, Hong et al., 2018a). The intrusive products at the northern margin of Junggar comprise diorites, quartz diorites, granodiorites and corresponding porphyries, biotite granites, and svenite or quartz syenite porphyries (Fig. 1b). Regional faults are prominent: the NW-trending Kalaxiang'er–Jieledikalatawu fault (F₁), the NW-trending Yulekenhalasu–Zhuolesay fault (F₂), the Mayinebo fault (F₃; the eastern section of the Irtysh Fault), and show shear deformation.

A series of Cu, Ni, Fe, and Au deposits, including mafic–ultramafic Cu–Ni, porphyry Cu–(Mo) and skarn Fe–Cu–Au deposits have been identified along the northern margin of the Junggar terrane since exploration commenced in the 1960s (Yang et al., 2012, Chen et al., 2018). The porphyry deposits are mainly found at the northern margin of the terrane and constitute the Kalaxian'gar Porphyry Copper Belt (KPCB). This belt includes Yuleken, Halasu I, Halasu II, Halasu III, Hayierken, Saketebaisayi, and Keziletawu porphyry deposits (Yang et al., 2012, Wu et al., 2015, Wu et al., 2018, Wu et al., 2019).

2.2. Yuleken porphyry Cu–Mo deposit

The Yuleken PCMD is situated at the northwestern margin of the KPCB (Hong et al., 2018a, Hong et al., 2018b) and it contains more than 0.2 Mt of copper with an average Cu grade of 1.04 % (Hong, 2017, Wu et al., 2015, Wu et al., 2018, Wu et al., 2019). The porphyry intrusions are hosted by the Middle Devonian Beitashan Formation and the Lower Carboniferous Jiangbasitao Formation (Yang et al., 2014, Hong et al., 2018a, Hong et al., 2018b; Fig. 2).

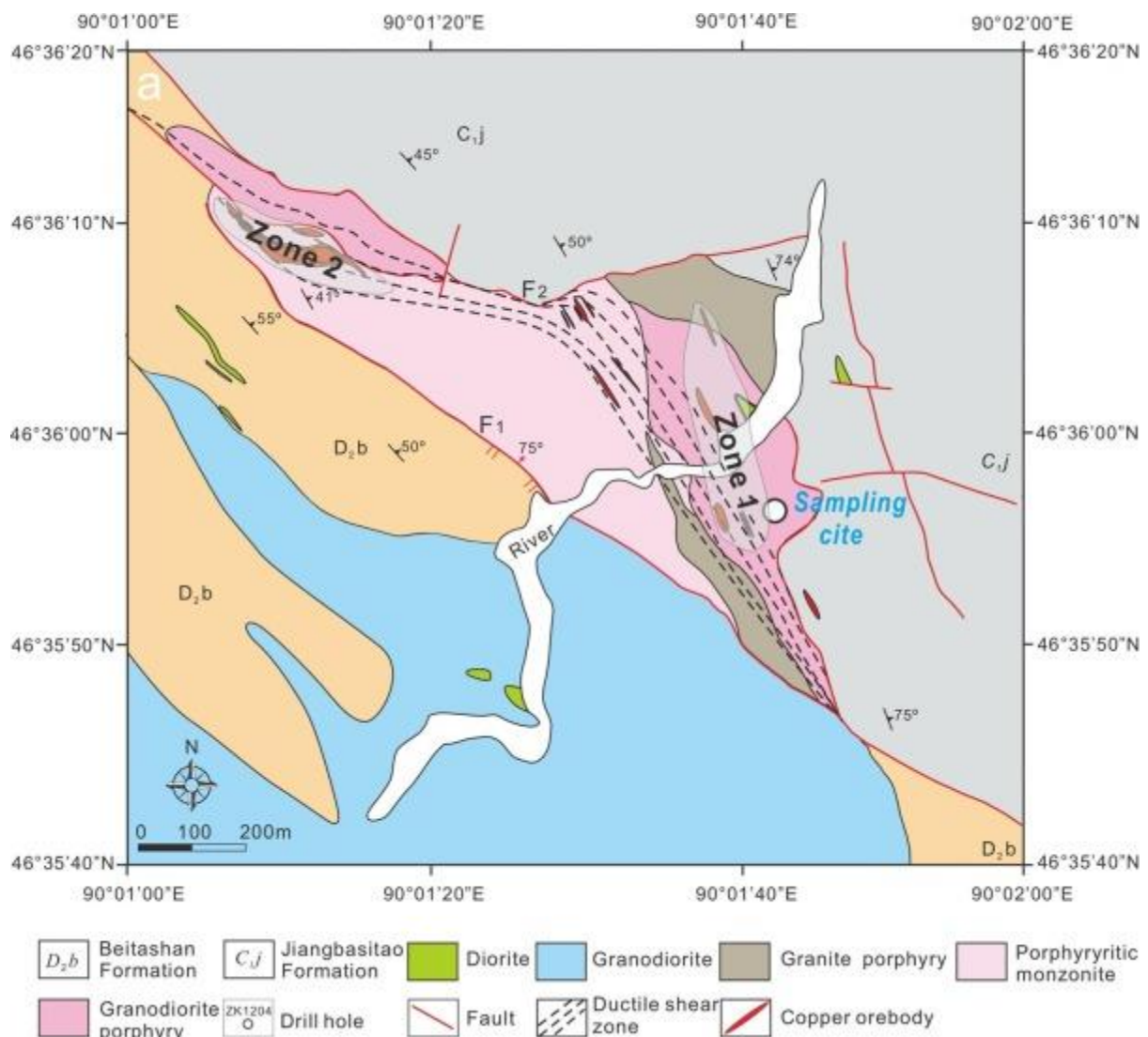


Fig. 2. Geological map of the Yuleken porphyry Cu–Mo deposit (modified after Xu et al., 2015, Yang et al., 2014, Hong et al., 2018a, Hong et al., 2018b).

The ore-bearing intrusions in the Yuleken PCMD range from porphyritic [monzonites](#) through granodiorites and granites, and generally range from Middle Devonian to Late Carboniferous age with a peak in [Late Devonian](#), which corresponds to the main mineralization stage ([Wu et al., 2015](#), [Hong et al., 2018a](#)). The granite porphyries occur as dykes and stocks in the interior and along the northwestern margin of the deposit, whereas the granodiorite and porphyritic monzonite occur in its southern and central portion ([Yang et al., 2014](#), [Hong et al., 2018a](#), [Hong et al., 2018b](#); [Fig. 2](#)). The irregularly shaped granite porphyry dykes and stocks generally strike 290–310° and are nearly 3 km long, 50–500 m wide, and southwest-dipping ([Yang et al., 2014](#)). The porphyritic monzonite occurs as an NW-trending stock, intruding clinopyroxene-phyric [basalts](#) of the Beitashan Formation ([Fig. 2](#)). The porphyritic monzonite is K-feldspar- and plagioclase-phyric, with a groundmass composed of quartz, [plagioclase](#), K-feldspar, and biotite ([Yang et al., 2014](#), [Wu et al., 2015](#), [Hong et al., 2018a](#), [Hong et al., 2018b](#)). The granodiorite porphyries are heterogeneously distributed and can be divided into two groups, one is distributed in the western part of the deposit, whereas the other in the central domain generally strikes 110–120° and shows relatively strong [mylonitization](#) ([Fig. 2](#)).

The mineralization in the Yuleken PCMD is spatially associated with the Late Devonian intrusive rocks and their host rocks. Mineralized porphyries in the Yuleken PCMD have undergone intense [hydrothermal alteration](#), including potassic, sericitic and propylitic style and [silicification](#). The alteration changes from potassic alteration and sericitization in the inner zone to the propylitic (chlorite-epidote-calcite) alteration in the outer zone. The potassic alteration comprises quartz, K-feldspar, and biotite overprinting original minerals, whereas the sericitic alteration is characterized by fine-grained quartz and sericite. The propylitic alteration is characterized by [epidote](#), chlorite, and [calcite](#) in the outer zone of the alteration system ([Xiang et al., 2012](#), [Yang et al., 2014](#), [Wu et al., 2015](#), [Xue et al., 2016](#)). The potassic and sericitic zones are intimately associated with Cu mineralization ([Xiang et al., 2012](#), [Yang et al., 2014](#), [Wu et al., 2015](#)). The [ore minerals](#) in the Yuleken PCMD are mainly [chalcocopyrite](#), [pyrite](#), and molybdenite, with minor [magnetite](#), [galena](#), and [pyrrhotite](#). Primary host mineral association includes quartz, [feldspar](#), biotite, and alteration phases are sericite, chlorite, epidote, calcite, and [gypsum](#). Ores have various textures including disseminations, veinlets, stockworks, and cataclastic [brittle deformation](#) ([Xiang et al., 2012](#), [Wu et al., 2015](#)).

Based on the alteration and mineralization style, the [ore deposit](#) can be divided into two zones: Zone 1 is located in the central and eastern part of the Yuleken PCMD and occurs as irregular strips that extend for about 800 m with a width of 20 to 120 m ([Yang et al., 2014](#)). Zone 2 comprises one larger and three smaller weakly deformed Cu-Au [ore bodies](#) ([Yang et al., 2014](#)) ([Fig. 2](#)). Cross-sections of the Yuleken PCMD show that a number of economic copper [sulfide](#) veins and minute molybdenite veins are associated with the mylonite/ultramylonite zones and their second-order structures ([Xiang et al., 2012](#), [Hong et al., 2018a](#), [Hong et al., 2018b](#)). The main Cu-Mo orebodies trend NW and dip to the NE. [Cleavage](#) domains are widely developed in the ductile deformed zone ([Xiang et al., 2012](#), [Xiang, 2013](#), [Hong et al., 2018a](#), [Hong et al., 2018b](#)).

The Yuleken PCMD alteration and mineralization occurred over at least three discrete events based on U-Pb, Re-Os, and Ar-Ar dating of the magmatic rocks, alteration and ore minerals ([Xiang, 2013](#), [Yang et al., 2014](#), [Xue et al., 2016](#), [Wu et al., 2015](#), [Wu et al., 2018](#), [Hong et al., 2018a](#), [Hong et al., 2018b](#)). The earliest monzonite to granite porphyry intrusions and mineralization formed from 391 to 372 Ma (U-Pb ages of primary [zircon](#) crystals; [Yang et al., 2012](#), [Yang et al., 2014](#), [Wu et al., 2015](#)); Re-Os dating of molybdenite from disseminated ores and veinlets in the granodioritic porphyry yielded ages of ca. 374–371 Ma ([Yang et al., 2012](#), [Xiang, 2013](#)), corresponding to a magmatic island arc setting. The [subduction](#) of the Paleo-Junggar (or Paleo-Asian) Ocean beneath the Junggar Plate induced formation of the Sawur island arc ([Yang et al., 2014](#)). The second event corresponds to a period of [ductile deformation](#) of granodiorite porphyries at 363–356 Ma (U-Pb ages of recrystallized zircon crystals in mylonitic rocks and Re-Os molybdenite ages from ductile deformed ores; [Xiang, 2013](#), [Hong et al., 2015](#), [Hong et al., 2017](#)). Dominant structures in the Yuleken PCMD comprise folded bedding (S₀), foliation (S₁), tension joints (S₂), and low-angle reverse faults (S₃) in the Kalaxian'gar area ([Fig. 3a–c](#); [Xiang et al., 2012](#), [Hong et al., 2017](#)). This deformation occurred in a syn- or late-collisional environment during the closure of the Paleo-Junggar Ocean ([Hong et al., 2015](#), [Hong et al., 2017](#)). The third event is recorded by sulfide mineralization and magmatic activities along cleavage planes which crosscut the foliations of [mylonite](#) at 335–320 Ma (ca. 334.5–331.5 Ma Re-Os model age of molybdenite; [Xiang et al., 2012](#), [Xiang, 2013](#); ca. 324–320 Ma U-Pb zircon ages of the granodiorite porphyry, which crosscuts the NW- to NNW-trending schistosity of the metasedimentary country rocks at a low angle; [Hong et al., 2017](#)) during post-collisional extension. The Ar-Ar dating of K-feldspar from K-feldspar-quartz-chalcocopyrite veins along the cleavage yielded ages of ca. 269 and ca. 199–198 Ma ([Xiang, 2013](#), [Xue et al., 2016](#)). The alteration ages correspond broadly to the three episodes of magmatic activity suggesting at least three overprinting porphyry mineralization events that are significantly separated in time ([Xiang et al., 2012](#)).

3. Sample description

The Yuleken PCMD experienced three mineralization events associated with magmatic-hydrothermal fluid release, ductile deformation, and cleavage formation ([Hong et al., 2018a](#), [Hong et al., 2018b](#)). Molybdenite samples were collected from the undeformed ore-bearing porphyry ([Fig. 4a,b](#)) with Cu grade from 0.25 to 0.79 %, Mo from 0.027 to 0.130 % (average: 0.06047%) and Au from 0.43 to 0.63 g/t ([Liu et al., 2010](#), [Yang et al., 2014](#)); the deformed molybdenite was acquired from areas with NW-trending foliations without fracture cleavage ([Fig. 4c,d](#)) with Mo grade 0.14 %; the hydrothermal molybdenite samples were taken along the late fracture cleavage planes where the Mo grade is 0.17 % ([Fig. 4e](#)).

Eight molybdenite samples come from drill hole ZK1204, which intersected typical undeformed porphyry with primary molybdenite (PM – ZK1204-1,2) during primary stage A (ca. 391–372 Ma), a zone of ductile deformation with deformed molybdenite (DM – ZK1204-3,4) and with recrystallized molybdenite within foliation (RM – ZK1204-5,6) during mylonitic stage B (ca. 363–356 Ma), and fracture-related mineralization with hydrothermal molybdenite (FM – ZK1204-7,8) during fracture cleavage stage C (ca. 335–320 Ma). In the undeformed porphyry, disseminated chalcocopyrite and molybdenite (PM) are [interstitial](#) to quartz, K-feldspar and plagioclase [phenocrysts](#), and to matrix minerals ([Fig. 4b](#)). The PM occurs as 50–250 μm large grains or aggregates with minor zoning in the [backscatter](#) electron (BSE) mode ([Fig. S1a](#)). This molybdenite variety has been subdivided

into two types: large euhedral crystals (150–250 μm) and smaller subhedral grains (50–100 μm). The mineralization within the ductile deformation domain is characterized by oriented clusters of pyrite, chalcopyrite, and molybdenite (DM) along the mylonitic foliation in the granodiorite porphyry (Fig. 4c,d). Some DM grains are strongly elongated and stretched, whereas some coarse-grained molybdenite within the foliation contains bright cores with primary growth zoning and mantles in the BSE mode (Fig. S1b). Fine-grained, lamellar molybdenite clusters (RM) occur in the pressure shadows of rotated quartz and K-feldspar porphyroclasts or crosscut the foliation at low angles suggesting that they are syn- or post-kinematic (Fig. 4d). The RM is composed of single wispy lamellae with common kinks and bending (Fig. S1c). The veins associated with the cleavage mineralization consist of molybdenite (FM) and magnetite adjacent to the wall rock, and chalcopyrite and pyrite in the center (Fig. 4e). The FM crystals are lamellar and have no zoning in BSE mode (Fig. S1d).

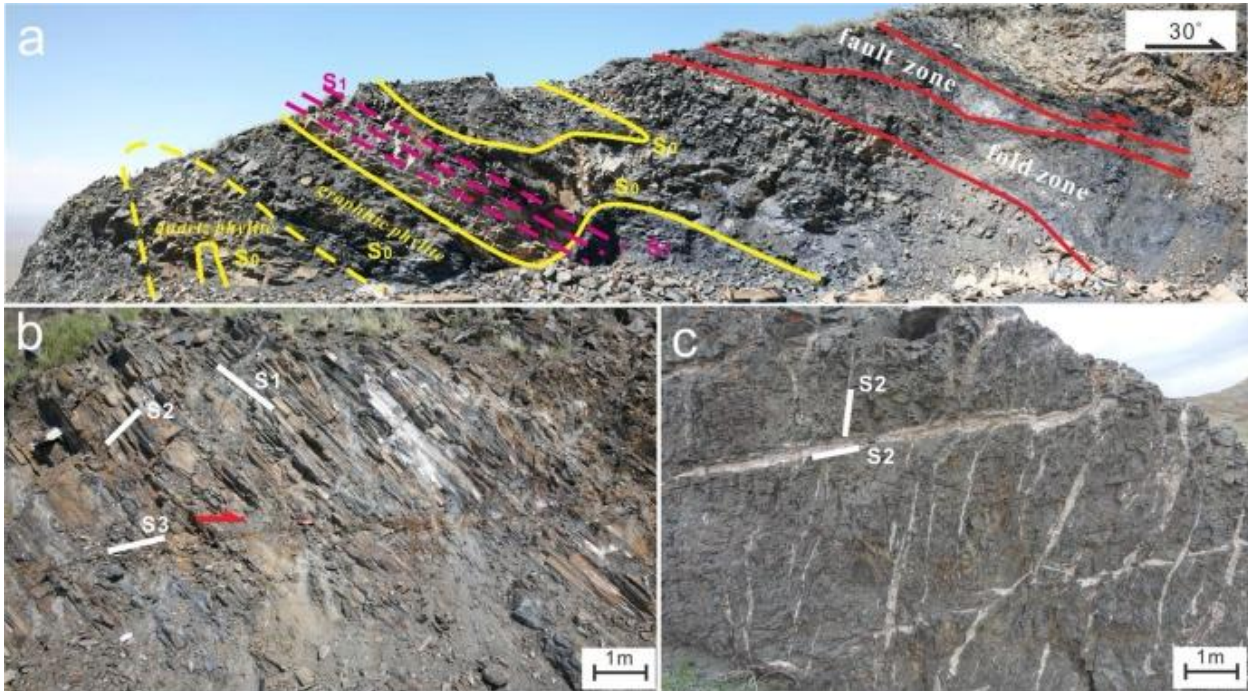


Fig. 3. Outcrop section displaying representative structures in the Yuleken PCMD (modified after [Hong et al., 2015](#), [Hong et al., 2017](#)). Structural features: S_0 – bedding, S_1 – foliation, S_2 – tension joints, S_3 – low-angle thrust fault. Detailed investigation of homogenization temperatures of [fluid inclusions](#) in the Yuleken PCMD has been performed by [Yang et al. \(2010\)](#) and [Xiang \(2013\)](#). The homogenization temperatures of fluids inclusions vary from 431 to 120 $^{\circ}\text{C}$, with three temperature peaks at 390, 290, and 190 $^{\circ}\text{C}$ ([Yang et al., 2010](#), [Xiang, 2013](#)). These might correspond to the early mineralization event in the Middle Devonian, which was closely related to porphyry systems with primary molybdenite as well as to the later superimposed tectonic-hydrothermal mineralization stages ([Yang et al., 2010](#), [Xiang, 2013](#), [Hong, 2017](#)).

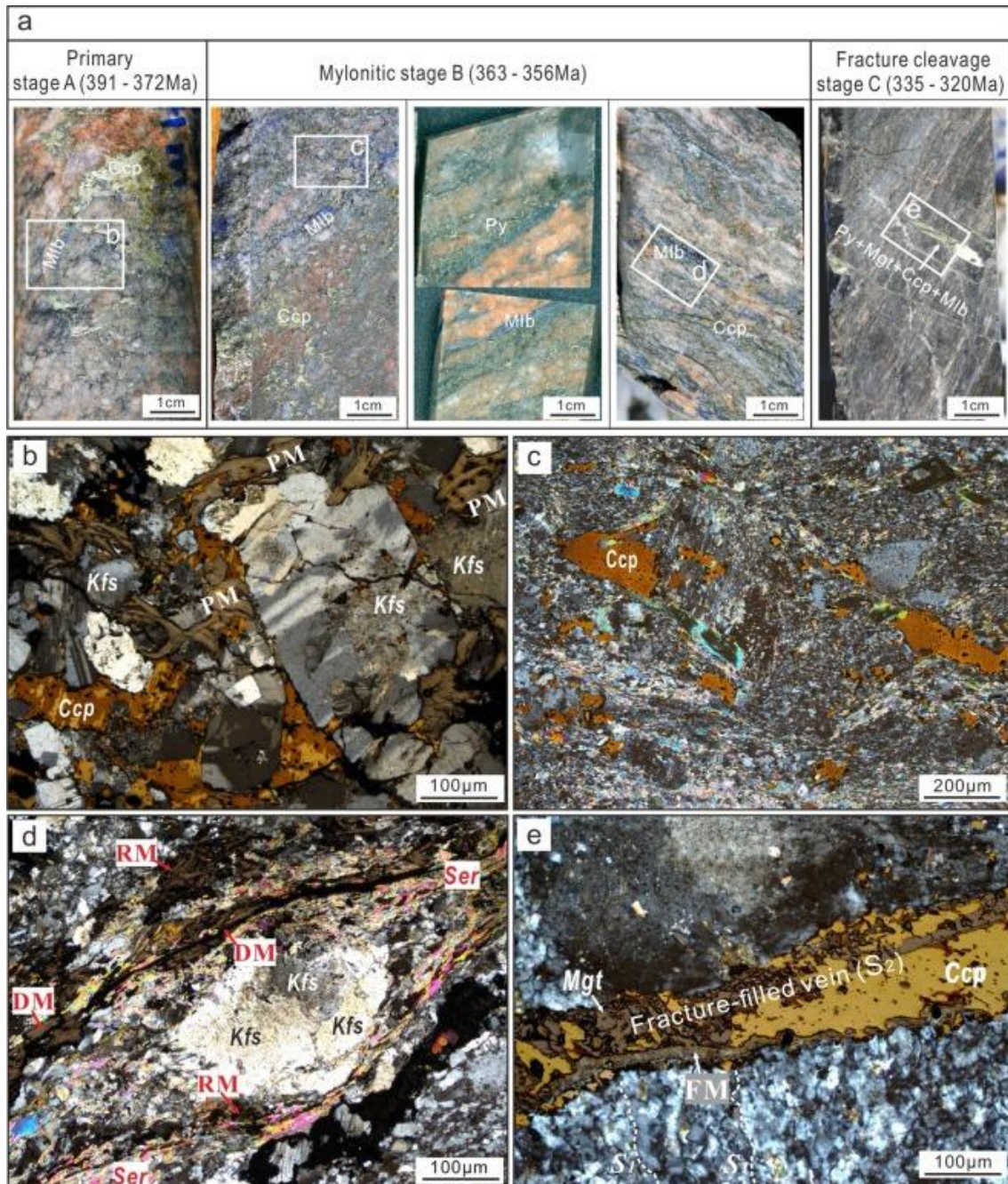


Fig. 4. *Mineralization* styles in the Yuleken porphyry Cu–Mo deposit: (a) primary porphyry mineralization (stage A); mineralization in foliated mylonitic rocks (stage B); vein mineralization in late *cleavage* planes (stage C); (b) euhedral *phenocrysts* predominately consisting of quartz, potassic-feldspar and *plagioclase* in *granodiorite* porphyry with *chalcopyrite* and *molybdenite*; (c, d) disseminated and recrystallized molybdenite (RM) and chalcopyrite aggregates in a *porphyroblast* trail suggesting their precipitation was contemporary with the *ductile deformation*; the deformed molybdenite (DM) is distributed along the deformed sericitized zone; (e) fine-grained or vein molybdenite (FM) distributed along late fracture cleavage; the cleavage planes have been replaced by *magnetite*, molybdenite, chalcopyrite, and *pyrite*. Abbreviations: Ccp – chalcopyrite; Mlb – molybdenite; Mgt – magnetite; Kfs – K-feldspar; Py – pyrite; Ser – sericite. S₁ – *foliation*; S₂ – *fracture cleavage*.

4. Methods

Major and trace elements were analyzed in all four molybdenite types. Concentrations of major elements were determined using the JEOL JXA-8200 Superprobe (EMP) at the GeoZentrum Nordbayern, University of Erlangen–Nürnberg (Tables 1 and S1). Reference materials and samples were analyzed in wavelength dispersive mode with a 20 kV acceleration voltage and a focused beam with a current of 20 nA. The following reference materials were used for molybdenite analyses: FeS₂ (Fe), CuFeS₂ (Cu, S), InAs (As), InSb (Sb), NiO (Ni), molybdenum metal (Mo), and cobalt metal (Co). Peak integration time was 20 s for Mo, Fe, and Ni, and 10 s for S, Cu, As and Sb. Detection limits for all elements are 0.01 wt%.

Table 1. Major and trace element composition of molybdenite from the Yuleken PCMD.

		EPMA (wt%)		LA-ICP-MS (ppm)						
ib (Type)	samples	S	Mo	Fe	Cu	Se	Te	V	Re	W
Er (PM)	ZK1204-1-1	40.41	58.32	561	1142	89.1	2.10	66.0	190	2.68
	ZK1204-1-2	40.52	58.12	1740	379	135	18.9	223	201	3.66
	ZK1204-1-3	40.80	58.51	258	400	86.4	0.581	32.6	188	3.13
	ZK1204-1-4	40.92	58.30	187	10.7	141	11.7	51.6	170	5.16
	ZK1204-1-5	40.51	58.41	386	500	92.9	0.572	13.9	187	5.68
	ZK1204-1-6	40.83	58.04	163	400	124	6.78	12.8	150	8.62
TH (PM)	ZK1204-2-1	40.31	57.62	650	440	BDL	BDL	6.77	116	31.5
	ZK1204-2-3	40.30	58.10	1159	506	BDL	BDL	BDL	170	32.6
	ZK1204-2-4	40.10	58.21	1161	1066	BDL	BDL	BDL	174	32.9
	ZK1204-2-5	40.80	58.51	200	380	149	BDL	BDL	145	124
	ZK1204-2-6	40.92	58.93	3134	500	68.0	BDL	BDL	127	18.0
	Average	40.58	58.28	344	391	111	6.78	30.6	165	24.3
	Min	40.10	57.62	163	10.7	68.0	0.57	6.77	116	2.68
	Max	40.92	58.93	650	506	149	18.9	66.0	201	124
Er (DM)	ZK1204-3-1	40.42	58.72	646	914	118	35.9	130	129	2.69
	ZK1204-3-2	40.71	58.61	942	87.0	93.5	2.80	24.3	100	3.94
	ZK1204-3-3	40.51	58.81	393	486	164	3.39	3.57	111	18.8
	ZK1204-3-4	39.92	58.80	291	179	160	3.35	8.37	100	12.6
	ZK1204-3-5	40.43	58.62	23.9	630	155	2.99	3.44	121	21.7
TH (DM)	ZK1204-3-6	40.02	58.22	200	440	320	BDL	BDL	104	42.9
	ZK1204-3-7	40.50	58.42	900	420	312	BDL	1.45	90.1	50.6
	ZK1204-3-8	39.92	58.61	240	879	BDL	BDL	BDL	93.2	187
	ZK1204-3-9	41.01	59.03	900	680	120	BDL	2.44	88.3	267
	ZK1204-3-10	41.41	59.04	270	200	138	BDL	3.64	98.0	264
	ZK1204-3-11	41.01	58.60	500	590	90.9	BDL	3.11	99.1	195
	Average	40.53	58.68	482	500	167	9.69	20.1	103	96.9
	Min	39.92	58.22	23.9	87.0	90.9	2.80	1.45	88.3	2.69
	Max	41.41	59.04	942	914	320	35.9	130	129	267
Er (RM)	ZK1204-5-1	40.92	58.91	3416	523	99.2	5.44	85.7	51.9	4.32
	ZK1204-5-2	40.10	58.83	119	635	78.6	2.56	110	82.5	1.88
	ZK1204-5-3	41.31	59.04	620	510	107	1.39	142	85.2	3.57
	ZK1204-5-4	40.51	58.92	110	131	88.9	1.19	172	72.8	2.07
	ZK1204-5-5	40.40	58.62	BDL	600	225	BDL	BDL	73.8	6.57
	ZK1204-5-6	40.64	58.71	450	580	300	BDL	BDL	72.9	6.26
	ZK1204-5-7	40.42	58.73	600	840	406	BDL	BDL	71.7	6.76
	ZK1204-5-8	41.12	59.74	200	BDL	BDL	BDL	BDL	63.5	131
TH (RM)	ZK1204-5-9	40.42	59.71	280	410	BDL	BDL	BDL	39.0	87.4
	ZK1204-5-10	41.11	59.72	760	340	420	BDL	BDL	52.1	17.0
	ZK1204-5-11	40.72	59.84	220	284	226	BDL	BDL	26.1	17.0
	ZK1204-5-12	40.10	60.10	1000	BDL	433	BDL	BDL	32.1	16.2
	ZK1204-5-13	39.91	59.91	100	1830	217	BDL	BDL	13.2	17.8
	ZK1204-5-14	40.82	59.91	109	177	237	BDL	BDL	22.7	17.5
	ZK1204-5-15	40.52	59.93	450	63.2	269	BDL	BDL	25.0	17.6

	ZK1204-5-16	40.30	59.90	BDL	550	290	BDL	BDL	18.8	16.6
	ZK1204-5-17	40.32	60.00	700	570	329	BDL	BDL	24.8	16.2
	Average	40.57	59.44	363	444	248	2.65	127	48.7	22.7
	Min	39.91	58.62	100	63.2	78.6	1.19	85.7	13.2	1.88
	Max	41.31	60.10	760	840	433	5.44	172	85.2	131
Er (FM)	ZK1204-7-1	40.32	60.10	114	740	87.4	0.781	161	3.62	7.41
	ZK1204-7-2	40.11	59.72	280	780	94.0	3.94	300	7.51	10.8
	ZK1204-7-3	40.30	60.21	1960	901	92.9	0.492	228	5.55	6.69
	ZK1204-7-4	40.70	59.61	351	701	83.5	4.06	29.7	22.3	2.86
	ZK1204-7-5	40.63	60.12	560	857	79.0	28.8	161	14.5	3.80
	ZK1204-7-6	40.71	59.71	234	670	93.0	7.70	123	8.20	6.56
	ZK1204-7-7	40.42	59.93	122	220	87.9	0.443	30.4	11.9	2.46
	ZK1204-7-8	40.51	59.91	501	82.1	84.8	0.444	35.7	15.5	2.57
	ZK1204-8-4	40.54	59.12	1390	490	105	4.58	149	28.1	4.56
	ZK1204-8-5	40.42	59.90	66.0	247	182	13.6	26.8	45.0	12.2
	ZK1204-8-6	40.42	59.21	281	388	99.7	0.592	137	29.0	2.97
	ZK1204-7-10	40.71	60.11	60.0	302	1090	BDL	BDL	15.0	9.61
	ZK1204-7-12	40.21	60.13	56.2	237	4354	BDL	BDL	6.95	12.2
TH (FM)	ZK1204-7-9	40.52	60.00	230	143	347	BDL	BDL	17.8	17.9
	ZK1204-7-11	40.31	60.10	69.0	663	1377	BDL	BDL	7.20	13.1
	ZK1204-7-13	40.60	60.12	470	733	BDL	BDL	BDL	21.8	11.4
	ZK1204-7-14	40.31	60.20	1800	880	BDL	BDL	BDL	8.17	9.44
	ZK1204-7-15	40.80	60.32	388	900	BDL	BDL	BDL	7.45	7.86
	ZK1204-7-16	40.64	60.33	311	600	BDL	BDL	BDL	10.5	7.81
	ZK1204-7-17	40.73	60.81	500	252	149	BDL	BDL	3.72	4.13
	ZK1204-7-18	40.41	60.40	340	BDL	139	BDL	BDL	1.86	5.40
	ZK1204-7-19	40.20	60.41	120	843	74.2	BDL	2.23	12.5	6.55
	ZK1204-8-3	40.61	59.22	256	10.0	120	2.54	234	30.0	5.94
	ZK1204-8-1	40.51	59.11	1176	481	104	10.3	165	24.2	3.99
	ZK1204-8-2	40.31	59.12	482	872	116	14.8	190	41.0	8.88
		Average	40.48	59.92	276	541	119	6.65	132	16.0
	Min	40.11	59.11	56.2	10.0	74.2	0.44	2.23	1.86	2.46
	Max	40.80	60.81	560	901	347	28.8	300	45.0	17.9

Abbreviations: *Primary porphyry mineralization stage (PM)*, *mineralization in foliated mylonitic rocks (DM and RM)*, and *fracture-related molybdenite (FM) of Yuleken PCMD*. *Er* - analyzed at the GeoZentrum Nordbayern, University of Erlangen-Nürnberg; *ETH* - analyzed at the Swiss Federal Institute of Technology. *BDL* - Below detection limit. *INCL* - contamination due to mineral inclusions.

Concentrations of trace elements in molybdenite were determined using a UP193FX laser and an Agilent 7500i ICP-MS at the GeoZentrum Nordbayern, University of Erlangen-Nürnberg. The laser operates with 193 nm wavelength and 15 Hz pulse frequency, and we used 20 s for background and for ablation analysis. The size of the ablation spot was 35 µm for the reference material and 25–35 µm for the samples. The irradiance and [fluence](#) were 0.79 GW/cm² and 3.91 J/cm², respectively. The following isotopes were measured: ⁵¹V, ⁵³Cr, ⁵⁷Fe, ⁵⁹Co, ⁶⁰Ni, ⁶³Cu, ⁶⁷Zn, ⁷¹Ga, ⁷⁵As, ⁷⁷Se, ¹⁰⁹Ag, ¹¹¹Cd, ¹¹⁵In, ¹¹⁸Sn, ¹²¹Sb, ¹²⁵Te, ¹⁸²W, ¹⁸⁵Re, ¹⁹⁷Au, ²⁰⁴Tl, ²⁰⁸Pb, and ²⁰⁹Bi. In order to avoid isobaric and polyatomic interferences the following isotopes were measured at two mass resolution modes: (1) the low mass resolution mode ($m/\Delta m = 300$) was used for ⁷⁵As, ⁷⁷Se, ¹⁰⁹Ag, ¹²¹Sb, ¹⁸²W, ¹⁸⁷Re, ²⁰⁸Pb, and ²⁰⁹Bi, whereas the medium resolution mode ($m/\Delta m = 4000$) mode was used for ⁵⁷Fe, ⁶³Cu and ⁶⁶Zn ([Pašava et al., 2016](#)). The [sulfide](#) standard (Fe, Ni)_{1-x}S (Re, Ni; [Wohlgemuth-Ueberwasser, 2007](#)) was used for external calibration for ¹⁸⁵Re and the Fe-Cu-Zn sulfide standard MASS-1 (USGS) ([Sylvester, 2008](#)) was used for external calibration for ⁵¹V, ⁵³Cr, ⁵⁷Fe, ⁵⁹Co, ⁶⁰Ni, ⁶³Cu, ⁶⁷Zn, ⁷¹Ga, ⁷⁵As, ⁷⁷Se, ¹⁰⁹Ag, ¹¹¹Cd, ¹¹⁵In, ¹¹⁸Sn, ¹²¹Sb, ¹²⁵Te, ¹⁸²W, ¹⁹⁷Au, ²⁰⁴Tl, ²⁰⁸Pb, and ²⁰⁹Bi. The standards NIST SRM 612 and NIST 610 were used as monitoring standards. The trace element concentrations were calculated using GLITTER ([Van Achterbergh et al., 2001](#)) and normalized to S as determined by [electron microprobe](#).

Additional analyses of trace elements in molybdenite were performed using a NexION 2000 (PerkinElmer, Canada/USA) fast-scanning [quadrupole mass spectrometer](#) coupled to a COMPex 102F (Coherent, Germany) ArF (193 nm) excimer [laser ablation](#) system at the ETH Zürich. Analyses were performed on four polished sections according to textural relations and intragranular zoning based on SEM-CL images. An in-house ablation cell designed to fit one section was used and fluxed with carrier gas consisting of high-purity He (11 L min^{-1}) to which sample gas consisting of high-purity Ar (10 L min^{-1}) was admixed downstream of the cell. A laser repetition rate of 10 Hz was used with a [crater](#) diameter of $40 \mu\text{m}$ and an on-sample [energy density](#) of ca. 7 J cm^{-2} for reference material and molybdenite samples. The ICP-MS instrument was optimized for maximum sensitivity on the entire mass range and low production of oxides ($^{248}\text{ThO}^+ / ^{232}\text{Th}^+ \leq 0.5 \%$). Data acquisition times for each spot were 30 s for background and 30 s during ablation. The following isotopes were measured: ^{51}V , ^{53}Cr , ^{57}Fe , ^{59}Co , ^{60}Ni , ^{63}Cu , ^{67}Zn , ^{71}Ga , ^{75}As , ^{77}Se , ^{109}Ag , ^{111}Cd , ^{115}In , ^{118}Sn , ^{121}Sb , ^{125}Te , ^{182}W , ^{185}Re , ^{197}Au , ^{204}Tl , ^{208}Pb , and ^{209}Bi . The sulfide standard GSE-1G was used to calibrate ^{182}W and ^{185}Re abundances and the Fe-Cu-Zn sulfide standard MASS-1 ([Jochum et al., 2011](#)) for the remaining isotopes as well as the primary external standard for quantification and instrumental drift correction by conventional standard-sample bracketing. We processed the LA-ICP-MS transient signals using the Matlab-based SILLS software ([Guillong et al. 2008](#)), with the detection limit calculation following [Pettke et al. \(2012\)](#), and normalized to Mo concentrations determined by electron microprobe. Inclusions or other defects were identified by examination of the time series of mass signals. We performed 45 analyses of trace elements in molybdenite, 13 analyses were discarded due to the presence of inclusions or analytical defects, and 32 analyses were used for further interpretation.

For further interpretation, all element concentrations were expressed as atoms per formula unit ($2 \text{ S} + \text{Se}$), that is, apfu or μapfu ([Table S2](#)). Consistency of electron microprobe and laser-ablation analyses was evaluated for several elements in the minor concentration range. [Figs. S2a,b](#) illustrate that the concentrations of representative elements (e.g., Fe and Cu) in molybdenite very closely follow 1:1 trend. Hence the two analytical approaches provide highly consistent data. Similarly, the LA-ICP-MS results for Fe and Cu acquired in Erlangen (Er) and ETH Zürich (ETH) at different analytical spots and arranged in order of increasing concentration narrowly cluster along the 1:1 trend ([Figs. S2c,d](#)). Comparison of the Re contents from the two laboratories indicates systematic discrepancy by 25 % ([Fig. S2e](#)), which, however, is substantially lower than the entire variation range, and it does not qualitatively affect any inferences. In [Fig. 5](#), the two measurement sets for all elements are distinguished for illustration and were merged in subsequent text and figures.

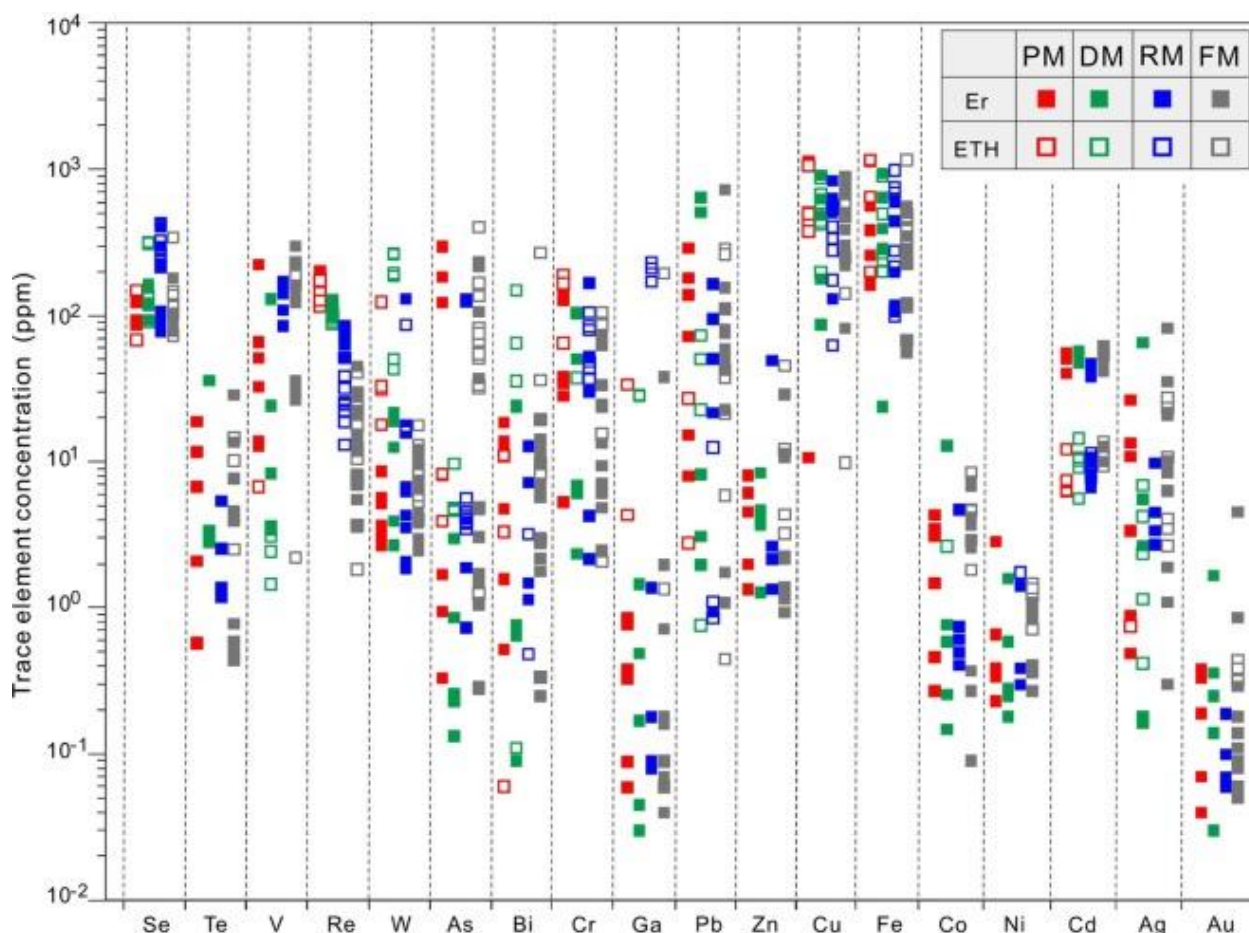


Fig. 5. Trace element concentrations in [molybdenite](#) from the Yuleken porphyry Cu-Mo deposit.

5. Results

Molybdenite departs variably from its ideal [stoichiometry](#) (MoS_2), and the Mo concentrations vary from 57.62 to 58.93 wt% (average: 58.28 wt%) in primary molybdenite (PM), 58.22 to 59.04 wt% (average: 58.68 wt%) in deformed molybdenite (DM), 58.62 to 60.10 wt% (average: 59.44 wt%) in recrystallized molybdenite (RM), and 59.11 to 60.81 wt% (average: 59.92 wt%) in hydrothermal molybdenite (FM) ([Table 1](#)). The S concentrations change from 40.10 to 40.92 wt% (average: 40.58 wt%) in PM, from 39.92 to 41.41 wt% (average: 40.53 wt%) in DM, from 39.91 to 41.31 wt% (average: 40.57 wt%) in RM, and from 40.11 to 40.80 wt% (average: 40.48 wt%) in FM ([Table 1](#)). Total trace element budget in molybdenite is 299–2789 ppm (excluding the data contaminated by inclusions) or up to 0.008 apfu ([Table S1](#)). The trace element budget remains essentially constant from primary through late hydrothermal molybdenite and is independent of the abundance of octahedral vacancies ([Fig. 6](#)).

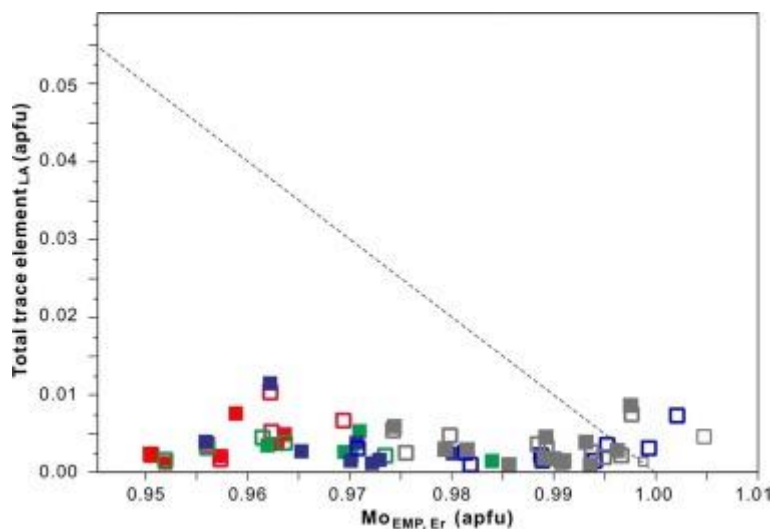


Fig. 6. Total trace element concentration vs. Mo abundance in molybdenite. The deviation from 1:1 trend (dashed line) suggests the formation of vacancy (defects) in high-temperature varieties of molybdenite.

Among analyzed trace elements, 74 % concentrations were found to be above the respective detection limits of LA-ICP-MS. In most analyses, Cr, Fe, Cu, Ge, As, Se, W, Re, Pb, and Bi are the most abundant trace elements ([Table 1](#)). The Se concentrations in molybdenites from the Yuleken deposits are broadly similar: 111 ppm in PM, 167 ppm in DM, 248 ppm in RM, and 119 ppm in FM ([Fig. 5](#); [Table 1](#)); some anomalously high concentrations (up to 4354 ppm Se in FM) may indicate presence of inclusions of Se-rich phases. The Te concentrations in the Yuleken molybdenites vary as follows (average values): 6.78 ppm (PM), 9.69 ppm (DM), 2.65 ppm (RM), and 6.65 ppm (FM) ([Fig. 5](#); [Table 1](#)). These concentrations are consistent with the concentration ranges from other mineralization types (greisen, base-metal, and porphyry deposits; [Pašava et al., 2016](#)).

The Re concentrations vary from 116 to 201 ppm (average: 165 ppm) in PM, from 88.3 to 129 ppm (average: 103 ppm) in DM, from 13.2 to 85.2 ppm (average: 48.7 ppm) in RM, and from 1.86 to 45.0 ppm (average: 16.0 ppm) in FM, thus displaying a decreasing trend from PM to FM ([Fig. 7](#); [Table 1](#)). The negative correlation between the Re and Mo can be fitted by a linear trend: $\text{Re (apfu)} = -0.0026 \text{ Mo (apfu)} + 0.00268$ ($R^2 = 0.613$) ([Fig. 7a](#)). The entire range of Re concentrations overlaps with that from porphyry Mo, Cu-Mo, and W-Mo deposits (see below), although the positive correlation of the Re contents in molybdenite with the Re-Os age of molybdenite at Yuleken ([Fig. 7c](#)), points to source or physico-chemical controls. The W concentrations in molybdenite are variable (1.88–267 ppm; [Table 1](#)) but independent of the textural type ([Fig. 7b](#)), and are most likely due to isomorphic substitution for molybdenum ([Ciobanu et al., 2013](#), [Pašava et al., 2015](#)). The above concentration range is similar to those from porphyry deposits and much lower than found in greisen-related and base-metal deposits ([Pašava et al., 2015](#), [Ren et al., 2018](#)).

Vanadium concentrations in individual molybdenite types increase from primary to late hydrothermal conditions (average values): 30.6 ppm in PM, 20.1 ppm in DM, 127 ppm in RM, and 132 ppm in FM ([Fig. 5](#); [Table 1](#)). The As concentrations in molybdenite up to 220 ppm are interpreted as substituents in the [crystal lattice](#), and compare favourably with those from [greisen](#), base-metal and porphyry deposits ([Pašava et al., 2016](#), [Plotinskaya et al., 2018](#), [Ren et al., 2018](#)). Peak As values (up to 407 ppm) are probably due to As-rich inclusions ([Table S1](#)). Time-resolved LA-ICP-MS depth profiles indicate some presence of Bi, Cr, Ga, and Pb in the form of impurities. The concentrations up to < 166 ppm Cr and 38 ppm Ga are probably due to element substitution, whereas anomalously high values (169–783 ppm Cr; 173–233 ppm Ga) are likely to represent inclusions of Cr- or Ga-rich phases ([Table S1](#)).

Zinc, copper and iron concentrations in the molybdenites from the Yuleken deposit are much lower than those from other porphyry deposits ([Plotinskaya et al., 2018](#), [Ren et al., 2018](#)). The very close correspondence between the Cu and Fe concentrations determined by EMP vs. LA-ICP-MS ([Figs. S2c,d](#)) indicates substitution in the crystal lattice. Several outliers (1066–1830 ppm Cu, 1000–3416 ppm Fe) point to the presence of nano-inclusions of other sulfide phases.

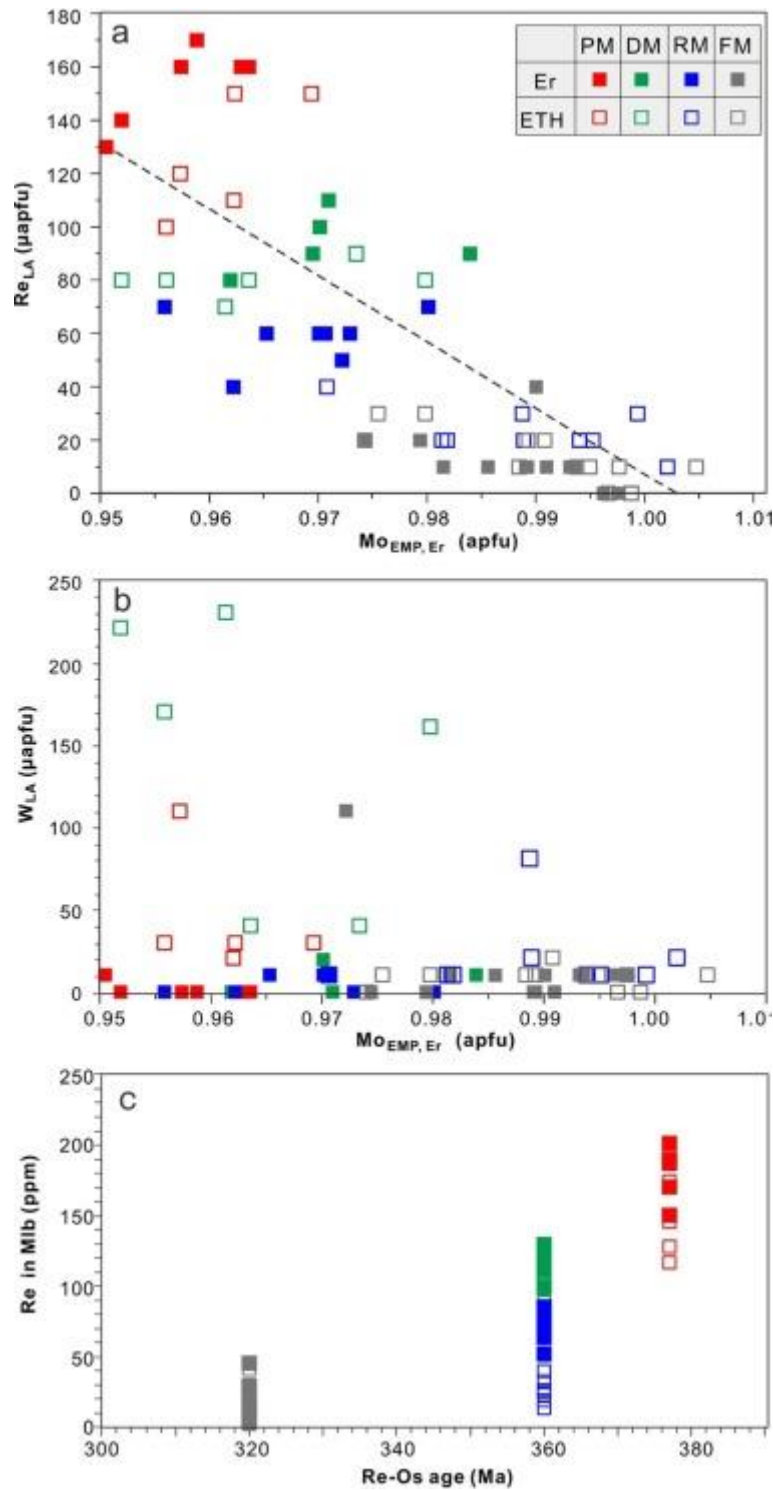


Fig. 7. Concentrations of Re, W and Mo in molybdenites from the Yuleken deposit: (a) Re vs. Mo show weak negative correlation, with a linear fit (black dotted line): $Re_{LA} (\text{apfu}) = -0.0026 Mo_{EMP} (\text{apfu}) + 0.00268$ ($R^2 = 0.613$); (b) W vs. Mo indicates no correlation and the W concentrations are independent of the molybdenite type; (c) Re in molybdenite vs. Re-Os age of molybdenite.

Cobalt, nickel, and gold show a relatively narrow range of concentrations, which are comparable to the Shapinggou porphyry molybdenum deposit (averages: 0.08 ppm Co, 2.06 ppm Ni; [Ren et al., 2018](#); [Table S3](#)). Cadmium and silver in the Yuleken molybdenites show irregular concentration variations that range over several orders of magnitude ([Table S1](#)) and some of the highest concentrations (60.7 ppm Cd; 82.1 ppm Ag) may be related to the presence of nanoscale or [microscale](#) inclusions as discussed extensively by [Pařava et al. \(2016\)](#).

6. Discussion

6.1. Physico-chemical controls on Re incorporation in molybdenite

Natural molybdenite occurs in two polytypes: 2H (common) and 3R (rare) (Newberry 1979). Samples from the porphyry Mo deposits from Canada and Australia are typically consistent with 2H-MoS₂ polytype with structural and metallic-like defects at significant concentrations varying between 0.1 and 10 % (Addou et al., 2015). Kulikova and Maksimiyuk (2013) and Ciobanu et al. (2013) also reported defects in the structure of Re-bearing molybdenite. Ciobanu et al. (2013) attributed high Re content to lattice defects in 2H-MoS₂. Thus, the lattice defects might have an impact on the Re distribution in molybdenite. Theoretically, molybdenite crystal with more defects can capture more Re (Shore and Fowler, 1996).

Molybdenite can theoretically incorporate Re⁴⁺ and W⁴⁺ in the Mo⁴⁺ site and Se²⁻ and Te²⁻ in the S²⁻ site, owing to the similarity of ionic radii (Shannon, 1976). Substitution of Re⁴⁺ and W⁴⁺ for Mo⁴⁺ was experimentally confirmed by Moh and Udubasa (1976), whereas replacement of S²⁻ by Se²⁻ and Te²⁻ was demonstrated by Drábek (1995). The concentrations of Se in all molybdenite types from the Yuleken PCMD have a similar range as those from the Kalinovskoe and Birgilda porphyry Cu deposits (Plotinskaya et al., 2018), Kalmakyr porphyry Cu-Mo-(Au) deposit (Pašava et al., 2015), but are much higher than those in molybdenite from the Shapingou porphyry Mo deposit (Ren et al., 2018; cf. Table S3). The Te contents at the Yuleken PCMD are very low (<35.9 ppm; Fig. 5), and there is lack of telluride or sulfotelluride inclusions based on time-resolved LA-ICP-MS spectra. This is consistent with the reported low concentrations (up to ~30 ppm) from diverse mineralization types (porphyry-, granite-, greisen-related, base metal-bearing; Pašava et al., 2015, Ren et al., 2018), but much lower than in molybdenite from the gold deposits (up to 112 ppm; Pašava et al., 2015; cf. Table S3). Overall, the Se and Te concentrations in the molybdenite from porphyry deposits are very low, but not limited by crystallochemical or saturation limits. The Se/S and Te/S ratios in molybdenite are probably dictated by the composition of parental media (hydrothermal fluids).

Rhenium in molybdenites from the Yuleken PCMD shows a broad negative correlation with Mo (Fig. 7a; Table S1), suggesting that cation vacancies in molybdenite promote the incorporation of Re. By contrast, the W concentrations in molybdenite are variable and independent of the textural type (Fig. 7b).

The Re contents in molybdenites are mainly affected by temperature (Giles and Schiling, 1972, Newberry, 1979, Xiong et al., 2006, Plotinskaya et al., 2018, Ren et al., 2018), redox conditions (Berzina et al., 2005, Plotinskaya et al., 2015), departures from ideal stoichiometry (Ciobanu et al., 2013, Kulikova and Maksimiyuk, 2013), and $f_{\text{HCl}}/f_{\text{HF}}$ (Xiong and Wood, 2001, Xiong and Wood, 2002, Berzina et al., 2005, Xiong et al., 2006). Previous studies of Xiong and Wood, 2001, Xiong and Wood, 2002, Xiong et al., 2006, Plotinskaya et al., 2018, Ren et al., 2018, and McFall et al. (2019) suggested that lower Re abundances in molybdenite correlate with low crystallization temperature. By contrast, the present study of individual genetic types of molybdenite at the Yuleken PCMD, supported by fluid inclusion microthermometry (Yang et al., 2010, Xiang, 2013, Hong, 2017), reveals a positive correlation between temperature and Re concentration in molybdenite. This is consistent with occurrences of Re-rich molybdenite in very high-temperature environments such as volcanic sublimates (Barton et al., 2020). An additional factor has been increasing oxygen fugacity from the primary porphyry to the ductile deformation stage (Hong et al., 2018b), consistent with increasing Re solubility in the fluid, hence its decreasing saturation in molybdenite (Plotinskaya et al., 2015).

6.2. Rhenium sources in porphyry deposits

Several hypotheses have been proposed for Re variation and enrichment in porphyry deposits: (i) subduction of anoxic sediments that carry high Re concentrations (Sun et al., 2003), documented by molybdenite samples with high Re contents from convergent margin volcanoes (Bernard et al., 1990); (ii) injection of Re-Au-bearing mafic magmas into ore-forming porphyry intrusions (Hattori and Keith, 2001). The positive correlation between Re and Au contents in porphyry deposits has been documented globally and related to the presence of mafic igneous phases (Sinclair and Jonasson, 2014). Porphyry Au, Cu-Au, Cu-Mo, and Cu deposits with high Re contents in molybdenite were predominantly derived from mantle magmatic components, and porphyry Mo and W-Mo deposits are mostly with low Re contents in molybdenite are dominated by crustal magmatic components (Fig. 8b,d). Consequently, high-Re molybdenites crystallize from magmatic-hydrothermal fluids originating from mantle-derived magmas, whereas low-Re molybdenites indicate crust-derived magmatic systems (Stein et al., 2001, Mao et al., 2006, Voudouris et al., 2009, Voudouris et al., 2013). Furthermore, the much lower Re contents in the molybdenite from the porphyry Mo deposits than those from the Cu-Mo deposits indicate that the mantle contribution to the porphyry Mo deposits is minor than in the case of the Cu-Mo deposits.

At the Yuleken deposit, the Re concentrations in molybdenite progressively decrease from 201 to 116 ppm in the primary porphyry-related mineralization (PM) through 129–13.2 ppm in ductile deformation zone during *syn*-collisional stage (DM, RM) and 45.0–1.86 ppm in fracture-related, late hydrothermal mineralization (FM) (Fig. 9). However, both the granodiorite porphyry and the mylonitized granodiorite porphyry have a mantle-derived affinity based on the Sr-Nd-Hf isotopic composition (Xiang, 2013, Yang et al., 2014). Thus, the Re depletion in molybdenite from the magmatic arc to *syn*-collisional stage is not controlled by changing magma source. Post-crystallization processes such as metamorphism (Stein 2006), deformation (Grabezhev and Voudouris, 2014) and hydrothermal alteration (McCandless et al., 1993, Suzuki et al., 2000) can induce Re loss and redistribution (Grabezhev and Shagalov, 2010). Here we propose that Re depletion in molybdenite observed in deformed and fracture-related hydrothermal molybdenites is related to the low-temperature hydrothermal processes.

6.3. Rhenium concentration in molybdenite vs. ore grade

Several studies have proposed empirical relationships between Re concentration in molybdenite and Mo, Cu or Au *ore grade* (Fleischer, 1959, Riley, 1967, Newberry, 1979, Barton et al., 2020). Compilation of Mo and Re abundances in porphyry deposits worldwide indicates that the Mo ore grade varies much less than the Re concentration in molybdenite (Fig. 8a,c; Table S4). Mathematically, this implies that increasing Re in molybdenite will lead to greater overall Re resource (in a deposit) and to lower overall Mo resource (in the same deposit), consistently with the observed trends (Fig. 8b,d; Table S4). Newberry, 1979, Berzina et al., 2005, Stein et al., 1997, Stein et al., 2001, and Selby and Creaser (2001) have attributed this correlation to dilution of Re by Mo as total Mo concentration increases from Cu and Cu-Au towards Mo porphyry systems. However, the dilution model cannot explain why the Mo-poor porphyry W-Mo systems lack Re-rich molybdenite (Fig. 8). Barton et al. (2020) suggested that Re concentration in molybdenite is governed by the efficiency of Re partitioning into the hydrothermal fluid and not by the Re content of its magmatic parent. Thus, the depletion of Re in molybdenites from the Mo-rich porphyry systems cannot be attributed to mass balance considerations alone.

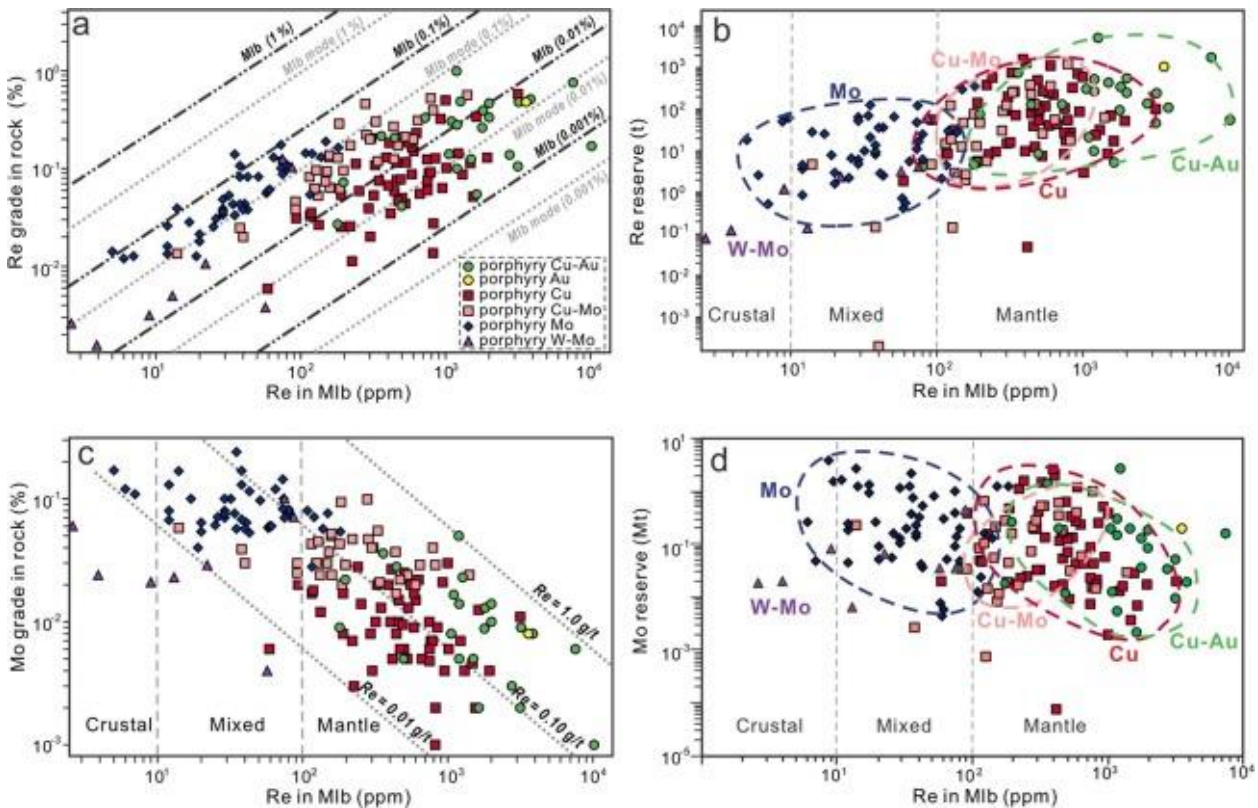


Fig. 8. (a) Re grade of porphyry deposits vs. average Re content of molybdenite; (b) Re reserve (t) of molybdenite vs. average Re content of molybdenite; (c) Mo grade of porphyry deposits vs. average Re content of molybdenite; (d) Mo reserve (Mt) of molybdenite vs. average Re content of molybdenite. Data from Sinclair et al. (2016) with our own updates. Mlb mode (%) = Mo grade (%) / 0.599. Data for the individual porphyry deposits are listed in Table S4.

6.4. Tectonic setting and metal enrichment processes in porphyry deposits

The Yuleken porphyry Cu-Mo deposit is located in the northern Saur oceanic island arc in the center of CAOB, south to the Zaysan-Irtysh suture zone (Yang et al., 2012, Chen et al., 2018). The Saur island arc was formed by the ocean-ocean southward subduction of the Zaysan-Irtysh oceanic plate beneath the Altay Terrane during Devonian. The porphyry Cu-Mo mineralization in the Saur oceanic island arc is genetically associated with 390–372 Ma porphyritic syenite, granodiorite porphyry and monzonitic porphyry (Xiang, 2013, Yang et al., 2014, Wu et al., 2015, Xue et al., 2016), and mainly occurs as disseminated, veinlet and stockwork mineralization at 374–371 Ma (Re-Os age of molybdenites; Xiang, 2013, Yang et al., 2014) with an average Mo grade of 0.060 % (Liu et al., 2010, Yang et al., 2014). The Sr-Nd-Hf data of the Late Devonian ore-bearing granitoids indicate that these are mainly derived from mantle-derived juvenile magmas (Xiang, 2013, Yang et al., 2014).

The collision of the Saur island arc and the Altay Terrane occurred at 367–356 Ma (Hong et al., 2017) and induced formation of 360 Ma mylonitized granodiorite porphyry, 355 Ma granitic gneiss and 354 Ma diorite porphyry in the Saur oceanic island arc (Hong et al., 2017). The Yuleken porphyry Cu-Mo deposit was metamorphosed and overprinted by ductile deformation at approximately 360 Ma (Xiang, 2013, Hong et al., 2015, Hong et al., 2017) during Saur-Altay arc collision, resulting in a concentration of Cu and Mo sulfide mineralization along foliation and formation of high-Cu lenticular orebodies. The deformed

and recrystallized granodiorite porphyry formed during this stage has a mantle-derived affinity (Sr-Nd-Hf isotope composition; [Xiang, 2013](#)). During this event, some Re has been leached from pre-existing molybdenite, whereas the bulk Mo ore grade increased (0.14 %) as a result of fluid focusing into deformation zones.

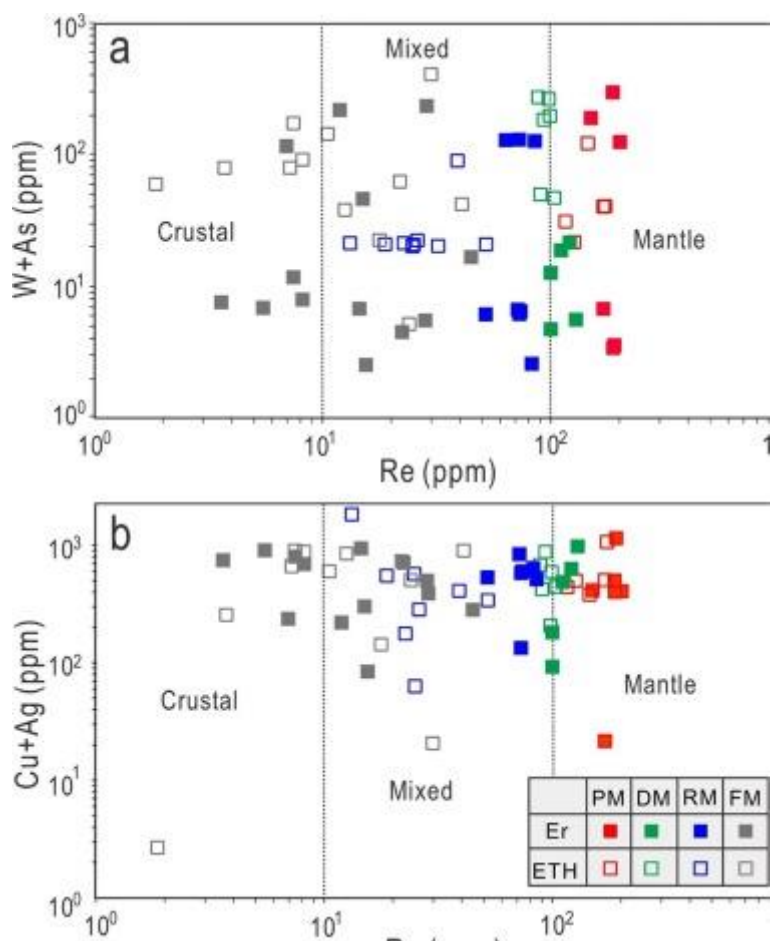


Fig. 9. Discrimination diagrams of (a) Re vs. (W + As) and (b) Re vs. (Cu + Ag) for molybdenite ([Pašava et al., 2016](#)), with analyses from the Yuleken deposit.

The Zaysan-Irtysh suture zone has evolved from compression to extension tectonic regime during post-collisional stage at 324–320 Ma ([Hong et al., 2017](#)), and the Yuleken porphyry district was overprinted and altered by cleavages with low-dip angles, some of which were filled by hydrothermal magnetite-sulfide veins crosscutting the foliations of mylonitized granodiorite porphyry (335–332 Ma Re-Os molybdenite age; [Xiang, 2013](#)). [Xue et al. \(2016\)](#) reported that the mantle-derived affinity of 266 Ma quartz monzonitic porphyry in Yuleken deposit based on Sr-Nd isotope data. We thus infer that this magmatic event has been sourced by mantle-derived magmas. During this event, the Mo ore grade has further increased to 0.17 %, and neighboring 327 Ma Xilekuduke porphyry Mo deposit ([Long et al., 2011](#)) and 305 Ma Suoerkuduke porphyry Cu-(Mo) deposit ([Wan et al., 2014](#)) formed during this post-collisional stage.

Individual generations of molybdenites in the Yuleken deposit (391–372, 365–363 and 335–320 Ma) have *in situ* Re contents of 165, 75.0 and 16.0 ppm, respectively, corresponding Mo ore grades from 0.07 through 0.14 and 0.17 %. Our study indicates that hydrothermal processes during syn- and late-collisional processes are responsible for progressively greater Mo enrichment in the host but depletion of Re in molybdenite. We thus argue that the heterogeneous distribution of Re in molybdenite and, in particular, Re depletion during successive hydrothermal events may be an indicator of Mo enrichment processes.

This trend appears to be universal during the transition from an island arc setting (mainly porphyry Cu-Mo mineralization) to a post-collisional stage (mainly porphyry Mo deposit) within the same [orogenic belt](#), as indicated by: (1) 525 ppm Re in molybdenite in the 323 Ma Tuwu-Yandong porphyry Cu-Mo deposit to 65.6 ppm of the 233 Ma giant Donggebi porphyry Mo deposit in the Jueluotage Belt ([Zhang et al., 2015](#), [Xiao et al., 2017](#)), (2) from 1416 ppm in the 477–476 Ma Duobaoshan porphyry Cu-Mo deposit ([Liu et al., 2017a](#)) and 737 ppm in the 470–471 Ma Tongshan porphyry Cu-Mo deposit ([Liu et al., 2017a](#)) to 13.6 ppm in the ~145 Ma giant Chalukou porphyry Mo deposit ([Liu et al., 2017b](#)) in the Great Xing'an belt, and (3) from 560 ppm in the 356 Ma Mikheevskoe porphyry Cu-Mo deposit to 22 ppm of the 299 Ma Talitsa porphyry Mo deposit in the Urals ([Tessalina and Plotinskaya, 2017](#)).

Most porphyry Mo deposits in the North China, Dabie Shan and South China orogens with proven reserves exceeding 15.3 Mt Mo have multiple Re-Os ages and the Re contents in molybdenite correlate positively with age (Chen et al., 2017a, Chen et al., 2017b, Chen et al., 2017c; Fig. 10a; Table S5), and this trend has been reported from other regions as well (e.g., Max and Endako porphyry Mo deposits in Canada, Malmberg and Flammefjeld giant porphyry Mo deposits in East Greenland; Brooks et al., 2004). Multiple magmatic events coeval with Mo mineralization events during successive *geodynamic* processes have been documented in the Northeast China orogen (Fig. 10b), the Dabie Shan orogen (Fig. 10c), and the South China orogen (Fig. 10d). The Northeast China orogen is considered to have undergone a long-term accretionary *orogeny* and growth of *continental crust* during Early Paleozoic, followed by Mesozoic to Cenozoic interaction with the Mongol-Okhotsk and Pacific oceanic plates (Chen et al., 2017c). As an example, the Chalukou giant porphyry Mo deposit in the Northeast China orogen at the northern margin of the Great Xing'an oceanic island arc in the CAOB, containing the largest total Mo reserve in the world, has 1.0 Ga *oceanic crust* basement (Li et al., 2014), and has been exposed to multiple complex tectonic-magmatic-mineralization processes, including: (1) oceanic island arc tectonism at 690 Ma related to southward intra-oceanic subduction of the South Mongolia Ocean (Li et al., 2014), (2) possible tectonic deformation associated with a collision between the Great Xing'an oceanic island arc and its northern opposite Erguna microcontinent at 516–511 Ma (Zhou et al., 2015), (3) *Ordovician* magmatic arc-related northward subduction of the Heihe oceanic plate (Li et al., 2014), resulting in the formation of the 477–476 Ma Duobaoshan porphyry Cu-Mo deposit about 165 km east of the Chalukou giant porphyry Mo deposit (Li et al., 2014) and 470–471 Ma Tongshan porphyry Cu-Mo deposit (Liu et al., 2017a), (4) ductile deformation associated with a collision between the Great Xing'an OIA and its southern opposite Baolidao oceanic island arc at 353 Ma (Liu et al., 2017b), and (5) multiple magmatic events and formation of the Chalukou giant porphyry Mo deposit in the *Early Jurassic* to *Early Cretaceous* period during intra-continental extension (Li et al., 2014). The intrusive hosts in the Chalukou area include 172–147 Ma monzogranites and *granite* porphyries, with multiple Mo mineralization events at 149–141 Ma (Li et al., 2014, Liu et al., 2017b). The multiple complex tectonic-magmatic-mineralization processes in Chalukou giant porphyry Mo deposit also display Re depletion in molybdenite, indicating that heterogeneous distribution of Re in molybdenite is related to multiple magmatic events during successive geodynamic events. We propose that reworking of mantle-derived porphyry systems by successive events of crustal growth may be the mechanism that promotes Mo enrichment, higher overall Mo ore grade, and eventually produces giant porphyry Mo deposits.

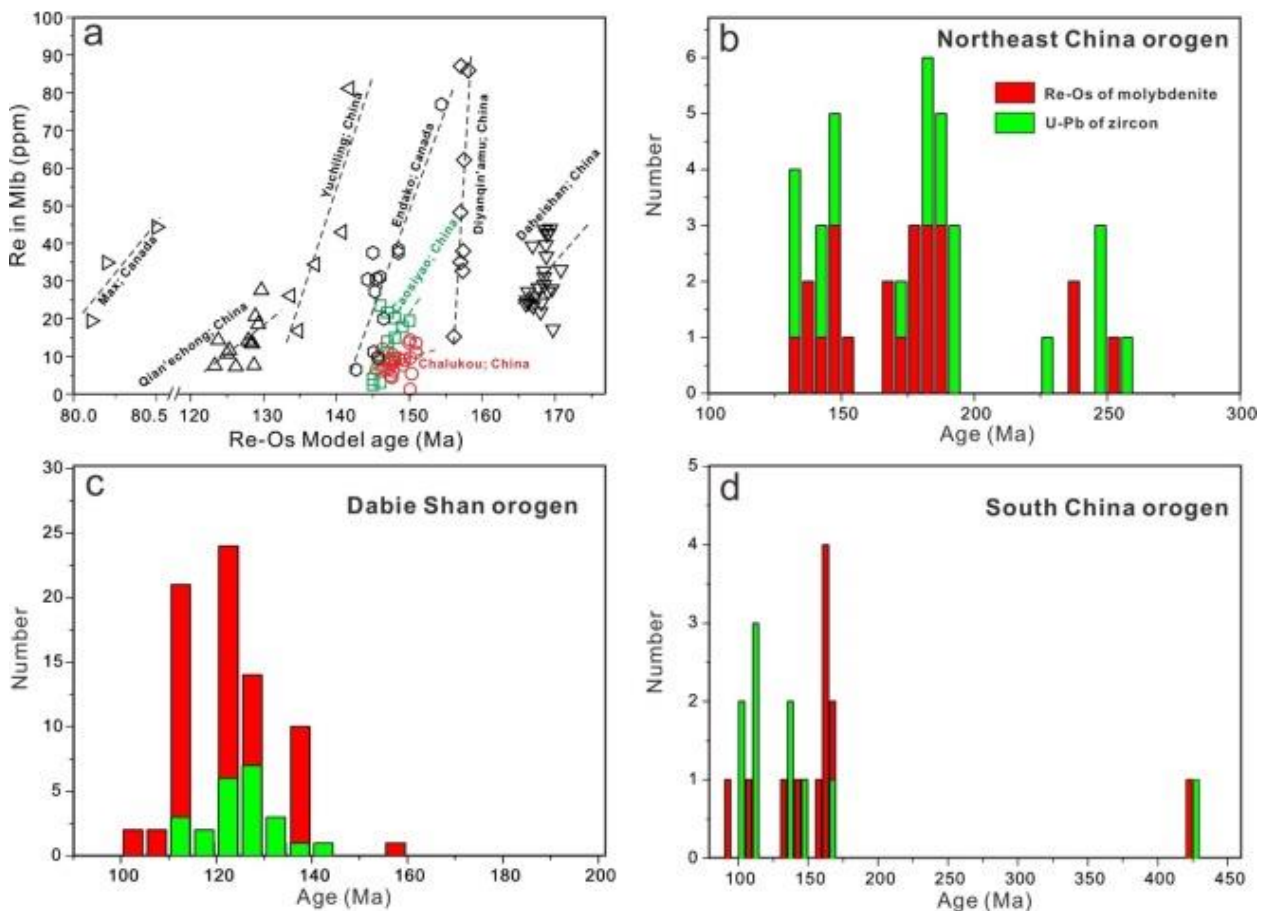


Fig. 10. Temporal trends of porphyry Mo deposits in the North China, Dabie Shan and South China orogens: (a) decreasing Re concentrations in molybdenite over time in the single porphyry Mo deposits; (b-d) distribution of Re-Os ages of molybdenite and U-Pb age of *zircon* of porphyry Mo deposits in the Northeast China orogen, Dabie Shan orogen, and South China orogen. Data for the individual porphyry deposits are listed in [Tables S5-S6](#).

7. Conclusions

We document new evidence for overprinting tectonic and magmatic activities that decrease Re contents in molybdenite and increase Mo grade of the Yuleken PCMD. Decreasing Re abundance in molybdenite is an indicator of increasing crustal contribution and/or decreasing crystallization temperature. Statistical analysis of published Re and Mo data from giant to small porphyry deposits worldwide shows several robust relationships between the Mo and Re grade and the Re contents in molybdenite:

$$\begin{aligned}\log(\text{Re grade in rocks}) &= 0.4986 \log(\text{Re in molybdenite}) - 2.258 \\ \log(\text{Mo grade in rocks}) &= -0.5065 \log(\text{Re in molybdenite}) - 0.4684 \\ \log(\text{Re reported resource}) &= 0.8219 \log(\text{Re in molybdenite}) - 0.489\end{aligned}$$

These relationships can be used to predict the Re and Mo grade of rocks and Re reserve using molybdenite composition. Furthermore, the Re concentration in molybdenite appear to be indicative of the bulk Cu/Mo ratio. Giant porphyry Mo deposits with low Re molybdenite were probably formed during multiple tectonic and magmatic events, with successively increasing crustal contribution.

Declaration of Competing Interest

The authors declare that they have no known competing financial interests or personal relationships that could have appeared to influence the work reported in this paper.

Acknowledgements

This research was jointly supported by the National Natural Science Foundation of China (Grant Nrs. [41802093](#) and [41390442](#)), the National Key R&D Program of China (Grant Nrs. [2017YFC0601201](#) and [2018YFC0604002](#)), the Fundamental Research Funds for the Central Universities, Sun Yat-sen University (2021qntd23), the Science and Technology Program of Guangzhou City (201906010030), the China Postdoctoral Science Foundation (Grant Nr. [2018M630201](#)), the 2018 Sino-German CSC-DAAD Postdoc Scholarship Program, the UCAS Joint PhD Training Program of China (2015/37), and Foundation of Key Laboratory of Mineral Resources, Institute of Geology and Geophysics, Chinese Academy of Sciences (KLMR2017-10). We acknowledge Florian Häckel and Thomas Günther for their support with the electron microprobe and Helene Brätz for her help with the laser ablation ICP-MS analyses in Erlangen. W. David Sinclair, Reiner Klemd, Kezhang Qin, Lianchang Zhang, Ping Shen, Qingdong Zeng, Mingjian Cao, Guangming Li, Peng Xiang, Malte Junge, Wolfgang Siebel, and Manuel Keith are thanked for their valuable discussions. We appreciate constructive comments from two journal reviewers.

References

- Addou, R., Colombo, L., Wallace, R.M., 2015. Surface defects on natural MoS₂. *Appl. Mater. Interface* 7, 11921–11929. Aud'etat, A., 2010. Source and evolution of molybdenum in the porphyry Mo (–Nb) deposit at Cave Peak, Texas. *J. Petrol.* 51 (8), 1739–1760.
- Barton, I.F., Rathkopf, C.A., Barton, M.D., 2020. Rhenium in molybdenite: a database approach to identifying geochemical controls on the distribution of a critical element. *Mining, Metallurgy Explor.* 37 (1), 21–37.
- Bernard, A., Symonds, R.B., Rose, W.I., 1990. Volatile transport and deposition of Mo, W and Re in high temperature magmatic fluids. *Appl. Geochem.* 5, 317–326.
- Berzina, A.N., Sotnikov, V.I., Economou-Eliopoulos, M., Eliopoulos, D.G., 2005. Distribution of rhenium in molybdenite from porphyry Cu-Mo and Mo-Cu deposits of Russia (Siberia) and Mongolia. *Ore Geol. Rev.* 26, 91–113.
- Brooks, C.K., Tegner, C., Stein, H., Thomassen, B., 2004. Re-Os and 40Ar/39Ar ages of porphyry molybdenum deposits in the East Greenland volcanic-rifted margin. *Econ. Geol.* 99, 1215–1222.
- Chen, H., Wan, B., Pirajno, F., Chen, Y., Xiao, B., 2018. Metallogensis of the Xinjiang Orogens, NW China-New discoveries and ore genesis. *Ore Geol. Rev.* 100, 1–11.
- Chen, Y.-J., Pirajno, F., Li, N., Deng, X.-H., 2017a. Molybdenum deposits in China. *Ore Geol. Rev.* 81, 401–404.
- Chen, Y.-J., Wang, P., Li, N., Yang, Y.-F., Pirajno, F., 2017b. The collision-type porphyry Mo deposits in Dabie Shan, China. *Ore Geol. Rev.* 81, 405–430.
- Chen, Y.-J., Zhang, C., Wang, P., Pirajno, F., Li, N., 2017c. The Mo deposits of Northeast China: a powerful indicator of tectonic settings and associated evolutionary trends. *Ore Geol. Rev.* 81, 602–640.
- Ciobanu, C.L., Cook, N.J., Kelson, C.R., Guerin, R., Kalleske, N., Danyushevsky, L., 2013. Trace element heterogeneity in molybdenite fingerprints stages of mineralization. *Chem. Geol.* 347, 175–189.
- Drabek, M., 1995. The Mo-Se-S and the Mo-Te-S systems, *Neues Jahrb. Mineral. Abh.* 169, 255–263. Fleischer, M., 1959. The geochemistry of rhenium, with special reference to its occurrence in molybdenite. *Econ. Geol.* 54, 1406–1413.
- Gao, J., Klemd, R., Zhu, M., Wang, X., Li, J., Wan, B.o., Xiao, W., Zeng, Q., Shen, P., Sun, J., Qin, K., Campos, E., 2018. Large-scale porphyry-type mineralization in the Central Asian metallogenic domain: a review. *J. Asian Earth Sci.* 165, 7–36.
- Giles, D.L., Schilling, J.H. 1972. Variation in rhenium content of molybdenite. In: *Proc. Internat. Geol. Congr. 24th Session, Section 10*, pp. 145–152.
- Glorie, S., De Grave, J., Buslov, M.M., Zhimulev, F.I., Izmer, A., Vandoorne, W., Ryabini, A., Van den haute, P., Vanhaecke, F., Elburg, M.A., 2011. Formation and Palaeozoic evolution of the Gorny-Altai–Altai-Mongolia suture zone (South Siberia): zircon U/Pb constraints on the igneous record. *Gondwana Res.* 20 (2-3), 465–484.
- Grabezhev, A.I., Shagalov, E.S., 2010. Rhenium distribution in molybdenite: results of microprobe scanning (copper porphyry deposits, the Urals). *Dokl. Earth Sci.* 431 (1), 351–355.
- Grabezhev, A.I., Voudouris, P.C., 2014. Rhenium distribution in molybdenite from the Vosnesensk porphyry Cu±(Mo, Au) deposit (southern Urals, Russia). *Can. Mineral.* 52, 671–686.
- Guillong, M., Meier, D.L., Allan, M.M., Heinrich, C.A., Yardley, B.W.D., 2008. SILLS. a Matlab-based program for the reduction of laser ablation ICP-MS data of homogeneous materials and inclusions. In: *Sylvester, P. (Ed.), Laser Ablation ICP-MS in the Earth Sciences: Current Practices and Outstanding Issues*. Mineral. Assoc. Canada Short Course Series, pp. 328–333.

- Hattori, K.H., Keith, J.D., 2001. Contribution of mafic melt to porphyry copper mineralization: evidence from Mount Pinatubo, Philippines, and Bingham Canyon, Utah, USA. *Mineral. Deposita* 36 (8), 799–806.
- Hong, T., 2017. Tectonic evolution and multiple prolonged mineralization of the Kalaxiagar porphyry copper deposit belt, Eastern Junggar. Ph. D. thesis. University of Chinese Academy of Sciences.
- Hong, T., Klemd, R., Gao, J., Xiang, P., Xu, X.-W., You, J., Wang, X.-S., Wu, C., Li, H., Ke, Q., 2017. The tectonic evolution of the Irtysh tectonic belt: New zircon U-Pb ages of arc-related and collisional granitoids in the Kalaxiagar tectonic belt, NW China. *Lithos* 272-273, 46–68.
- Hong, T., Xiang, P., You, J., Zhang, L.C., Wu, C., Wu, Q., Xu, X.W., 2015. Texture and formation age of the eastern Irtysh collision belt. *Acta Petrol. Sin.* 31, 571–593 (in Chinese with English abstract).
- Hong, T., Xu, X.-W., Gao, J., Peters, S.G., Li, J., Cao, M., Xiang, P., Wu, C., You, J., 2018a. Element migration of pyrites during ductile deformation of the Yuleken porphyry Cu deposit (NW-China). *Ore Geol. Rev.* 100, 205–219.
- Hong, T., Xu, X., You, J., Wu, C., Li, H., Ke, Q., 2018b. Cu and Mo re-enrichment during ductile deformation: a case study of the Yuleken porphyry Cu deposit, Eastern Junggar, NW China. *J. Asian Earth Sci.* 165, 285–304.
- Jochum, K.P., Weis, U., Stoll, B., Kuzmin, D., Yang, Q., Raczek, I., Jacob, D.E., Stracke, A., Birbaum, K., Frick, D.A., 2011. Determination of reference values for NIST SRM 610–617 glasses following ISO guidelines. *Geostand. Geoanal. Res.* 35, 397–429.
- Kulikova, I.M., Maksimuk, I.E., 2013. Morphological study of species of admixture atoms in the crystal structure of molybdenite. *New Data Miner.* 48, 71–81.
- Li, N., Pirajno, F., 2017. Early Mesozoic Mo mineralization in the Qinling Orogen: an overview. *Ore Geol. Rev.* 81, 431–450.
- Li, Z.-Z., Qin, K.-Z., Li, G.-M., Ishihara, S., Jin, L.-Y., Song, G.-X., Meng, Z.-J., 2014. Formation of the giant Chalukou porphyry Mo deposit in northern Great Xing'an Range, NE China: Partial melting of the juvenile lower crust in intra-plate extensional environment. *Lithos* 202-203, 138–156.
- Liu, G., Dong, L., Xue, C., Li, X., Zhang, L., Wei, G., He, L., Zhao, Z., Qin, J., Zhang, Z., 2010. Geological characteristics and exploration direction of the Yulekenhalasu copper deposit, Xinjiang. *Xinjiang Geol.* 28, 377–384 (in Chinese with English abstract).
- Liu, J., Li, Y., Zhou, Z.-H., OuYang, H.-G., 2017a. The Ordovician igneous rocks with high Sr/Y at the Tongshan porphyry copper deposit, satellite of the Duobaoshan deposit, and their metallogenic role. *Ore Geol. Rev.* 86, 600–614.
- Liu, Y., Bagas, L., Jiang, S., Wang, F., 2017b. The Chalukou deposit in the North Great Xing'an Range of China: a protracted porphyry Mo ore-forming system in a long-lived magmatic evolution cycle. *Ore Geol. Rev.* 89, 171–186.
- Long, L., Wang, Y., Du, A., Wang, J., Wang, L., Wang, S., Pu, K., Qu, W., 2011. Molybdenite Re-Os age of Xilekuduke Cu-Mo deposit in Xinjiang and its geological significance. *Mineral Deposits* 30, 635–644 (in Chinese with English abstract).
- Long, X., Yuan, C., Sun, M., Xiao, W., Zhao, G., Wang, Y., Cai, K., Xia, X., Xie, L., 2010. Detrital zircon ages and Hf isotopes of the early Paleozoic flysch sequence in the Chinese Altai, NW China: new constrains on depositional age, provenance and tectonic evolution. *Tectonophysics* 480 (1-4), 213–231.
- Mao, J., Wang, Y., Lehmann, B., Yu, J., Du, A., Mei, Y., Li, Y., Zang, W., Stein, H.J., Zhou, T., 2006. Molybdenite Re-Os and albite ⁴⁰Ar/³⁹Ar dating of Cu-Au-Mo and magnetite porphyry systems in the Yangtze River valley and metallogenic implications. *Ore Geol. Rev.* 29 (3-4), 307–324.
- McCandless, T.E., Ruiz, J., Campbell, A.R., 1993. Rhenium behavior in molybdenite in hypogene and near-surface environments: Implications for Re-Os geochronometry. *Geochim. Cosmochim. Acta* 57 (4), 889–905.
- McFall, K., Roberts, S., McDonald, I., Boyce, A.J., Naden, J., Teagle, D., 2019. Rhenium enrichment in the Muratdere Cu-Mo (Au-Re) porphyry deposit, Turkey: evidence from stable isotope analyses ($\delta^{34}\text{S}$, $\delta^{18}\text{O}$, δD) and laser ablation-inductively coupled plasma-mass spectrometry analysis of sulfides. *Econ. Geol.* 114, 1433–1466.
- Mi, M., Chen, Y.-J., Yang, Y.-F., Wang, P., Li, F.-L., Wan, S.-Q., Xu, Y.-L., 2015. Geochronology and geochemistry of the giant Qian'echong Mo deposit, Dabie Shan, eastern China: implications for ore genesis and tectonic setting. *Gondwana Res.* 27 (3), 1217–1235.
- Moh, G.H., Udubasa, G., 1976. Molybdenit-Tungstenit-Mischkristalle und Phasenrelationen im System Mo-W-S. *Chem. Erde* 35, 327–335.
- Morris, D.F.C., Short, E.L., 1969. Rhenium. In: Wedepohl, K.H. (Ed.), *Handbook of Geochemistry II-1*. Springer, Berlin, p. 75.
- Newberry, R.J.J., 1979. Polyttypism in molybdenite (II): relationships between polytypism, ore deposition/alteration stages and rhenium contents. *Am. Mineral.* 64, 768–775.
- Pasava, J., Veselovský, F., Drábek, M., Svojtka, M., Pour, O., Klomínský, J., Škoda, R., Ďurišová, J., Ackerman, L., Halodov'á, P., Haluzov'á, E., 2015. Molybdenite–tungstenite association in the tungsten-bearing topaz greisen at Vítkov (Krkonoše-Jizera Crystalline complex, Bohemian Massif): indicator of changes in physico-chemical conditions in mineralizing system. *J. Geosci.* 60, 149–161.
- Pasava, J., Svojtka, M., Veselovský, F., Ďurišová, J., Ackerman, L., Pour, O., Drábek, M., Halodov'á, P., Haluzov'á, E., 2016. Laser ablation ICPMS study of trace element chemistry in molybdenite coupled with scanning electron microscopy (SEM) – an important tool for identification of different types of mineralization. *Ore Geol. Rev.* 72, 874–895.
- Pettke, T., Oberli, F., Audétat, A., Guillong, M., Simon, A.C., Hanley, J.J., Klemm, L.M., 2012. Recent developments in element concentration and isotope ratio analysis of individual fluid inclusions by laser ablation single and multiple collector ICP-MS. *Ore Geol. Rev.* 44, 10–38.
- Plotinskaya, O.Y., Grabezhev, A.I., Seltmann, R., 2015. Rhenium in ores of the Mikheevskoe porphyry Cu-Mo deposit, South Urals. *Geol. Ore Deposits* 57 (2), 118–132.
- Plotinskaya, O.Y., Abramova, V.D., Groznova, E.O., Tessalina, S.G., Seltmann, R., Spratt, J., 2018. Trace-element geochemistry of molybdenite from porphyry Cu deposits of the Birgilda-Tomino ore cluster (South Urals, Russia). *Mineral. Mag.* 82 (S1), S281–S306.
- Ren, Z., Zhou, T., Hollings, P., White, N.C., Wang, F., Yuan, F., 2018. Trace element geochemistry of molybdenite from the Shapinggou super-large porphyry Mo deposit, China. *Ore Geol. Rev.* 95, 1049–1065.
- Richards, J.P., 2011. Magmatic to hydrothermal metal fluxes in convergent and collided margins. *Ore Geol. Rev.* 40, 1–26.
- Riley, G.H., 1967. Rhenium concentration in Australian molybdenites by stable isotope dilution. *Geochim. Cosmochim. Acta* 31, 1489–1497.
- Shannon, R.D., 1976. Revised effective ionic radii and systematic studies of interatomic distances in halides and chalcogenides. *Acta Crystallogr. A* 32, 751–767.
- Shore, M., Fowler, A.D., 1996. Oscillatory zoning in minerals: A common phenomenon. *Can. Mineral.* 34, 1111–1126.
- Sinclair, W.D., Jonasson, I.R., 2014. Highly siderophile elements (Re, Au and PGE) in porphyry deposits and their mantle origins. *Acta Geol. Sinica* 88 (s2), 616–618.
- Sinclair, W.D., Jonasson, I.R., Kirkham, R.V. and Soregaroli, A.E., (2016. Rhenium in Canadian mineral deposits, Open File 7780, 58 p.
- Stein, H.J., 2006. Low-rhenium molybdenite by metamorphism in northern Sweden: recognition, genesis, and global implications. *Lithos* 87 (3-4), 300–327.
- Stein, H.J., Maarkey, R.J., Morgan, J.W., Du, A.D., Sun, Y., 1997. Highly precise and accurate Re-Os ages for molybdenite from the East Qinling Molybdenum Belt, Shaanxi Province, China. *Econ. Geol.* 92, 827–835.
- Stein, H.J., Markey, R.J., Morgan, J.W., Hannah, J.L., Schersten, A., 2001. The remarkable Re-Os chronometer in molybdenite: how and why it works. *Terra Nova* 13 (6), 479–486.
- Selby, D., Creaser, R., 2001. Re-Os geochronology and systematics in molybdenite from the Endako porphyry molybdenum deposit, British Columbia, Canada. *Econ. Geol.* 96, 197–204.
- Sun, M., Yuan, C., Xiao, W., Long, X., Xia, X., Zhao, G., Lin, S., Wu, F., Kröner, A., 2008. Zircon U-Pb and Hf isotopic study of gneissic rocks from the Chinese Altai: progressive accretionary history in the early to middle Palaeozoic. *Chem. Geol.* 247 (3-4), 352–383.
- Sun, W., Arculus, R.J., Bennett, V.C., Eggins, S.M., Binns, R.A., 2003. Evidence for rhenium enrichment in the mantle wedge from submarine arc-like volcanic glasses (Papua New Guinea). *Geology* 31 (10), 845. <https://doi.org/10.1130/G19832.1>.

- Suyehiro, K., Takahashi, N., Ariei, Y., Yokoi, Y., Hino, R., Shinohara, M., Kanazawa, T., Hirata, N., Tokuyama, H., Taira, A., 1996. Continental crust, crustal underplating, and low-Q upper mantle beneath an oceanic island arc. *Science* 272 (5260), 390–392.
- Suzuki, K., Kagi, H., Nara, M., Takano, B., Nozaki, Y., 2000. Experimental alteration of molybdenite: evaluation of the Re–Os system, infrared spectroscopic profile and polytype. *Geochim. Cosmochim. Acta* 64 (2), 223–232.
- Sylvester, P.J., 2008. Matrix effects in laser ablation-ICP-MS. In: Sylvester, P. (Ed.), *Laser Ablation ICP-MS in the Earth Sciences: Current Practices and Outstanding Issues*. Mineralogical Association of Canada, Short Course Series, pp. 67–78.
- Tessalina, S.G., Plotinskaya, O.Y., 2017. Silurian to Carboniferous Re–Os molybdenite ages of the Kalinovskoe, Mikheevskoe and Talitsa Cu-and Mo porphyry deposits in the Urals: Implications for geodynamic setting. *Ore Geol. Rev.* 85, 174–180.
- Van Achterbergh, E., Ryan, C., Jackson, S., Griffin, W.L., 2001. Appendix 3: Data reduction software for LA-ICP-MS. In: Sylvester, P. (Ed.), *Laser Ablation-ICPMS in the Earth Sciences*. Mineral. Assoc. Canada Short Course, pp. 239–243.
- Voudouris, P., Melfos, V., Spry, P.G., Bindi, L., Kartal, T., Arikas, K., Moritz, R., Orтели, M., 2009. Rhenium-rich molybdenite and rheniite (ReS₂) in the Pagoni Rach- Kirki Mo–Cu–Te–Ag–Au deposit northern Greece: implications for the rhenium geochemistry of porphyry-style Cu-Mo and Mo mineralization. *Can. Mineral.* 47, 1013–1036.
- Voudouris, P., Melfos, V., Spry, P., Bindi, L., Moritz, R., Orтели, M., Kartal, T., 2013. Extremely Re-rich molybdenite from porphyry Cu-Mo–Au prospects in Northeastern Greece: mode of occurrence, causes of enrichment, and implications for gold exploration. *Minerals* 3 (2), 165–191.
- Wohlgenuth-Ueberwasser, C.C., 2007. Synthesis of PGE sulfide standards for laser ablation inductively coupled plasma mass spectrometry (LA-ICP-MS). *Contrib. Mineral. Petr.* 154, 607–617.
- Wan, B.o., Xiao, W., Han, C., Windley, B.F., Zhang, L., Qu, W., Du, A., 2014. Re–Os molybdenite age of the Cu-Mo skarn ore deposit at Suoerkuduke in East Junggar, NW China and its geological significance. *Ore Geol. Rev.* 56, 541–548.
- Wu, C., Chen, H., Hollings, P., Xu, D., Liang, P., Han, J., Xiao, B., Cai, K., Liu, Z., Qi, Y., 2015. Magmatic sequences in the Halasu Cu Belt, NW China: Trigger for the Paleozoic porphyry Cu mineralization in the Chinese Altay-East Junggar. *Ore Geol. Rev.* 71, 373–404.
- Wu, C., Chen, H., Liang, P., Han, J., Liu, Z., Fang, J., Xu, D., 2018. Paragenesis and fluid evolution of the Halasu III porphyry Cu deposit, East Junggar (NW China): Implications for the Paleozoic multiphase superimposing mineralization in the Central Asian Orogenic Belt. *Ore Geol. Rev.* 100, 183–204.
- Wu, C., Chen, H., Hong, W., Li, D., Liang, P., Fang, J., Zhang, L., Lai, C., 2019. Magnetite chemistry and implications for the magmatic-hydrothermal ore-forming process: An example from the Devonian Yuleken porphyry Cu system, NW China. *Chem. Geol.* 522, 1–15.
- Xiang, P., 2013. Geological Characteristics, Metallogenic Epoch and Its Evolution Process of the Superimposed and Tectonic Reworked Porphyry Cu-Mo Deposits in the Kalaxianger Porphyry Copper Belt, Eastern Junggar. University of Chinese Academy of Sciences. Ph. D. thesis.
- Xiang, P., Zhang, L.C., Xu, X.W., Liu, G.R., Liu, Z.J., Jin, X.D., Li, W.J., 2012. Geological characteristics and genesis of Yuleken-Halasu superimposed and tectonically reworked porphyry copper-gold (molybdenum) deposit in Qinghe, Xinjiang. *Acta Petrol. Sin.* 28, 2369–2380 (in Chinese with English abstract).
- Xiao, B., Chen, H., Hollings, P., Han, J., Wang, Y., Yang, J., Cai, K., 2017. Magmatic evolution of the Tuwu-Yandong porphyry Cu belt, NW China: constraints from geochronology, geochemistry and Sr–Nd–Hf isotopes. *Gondwana Res.* 43, 74–91.
- Xiong, Y., Wood, S.A., 2001. Hydrothermal transport and deposition of rhenium under subcritical conditions (up to 200°C) in light of experimental studies. *Econ. Geol.* 96, 1429–1444. Xiong, Y., Wood, S.A., 2002. Experimental determination of the hydrothermal solubility of ReS₂ and the Re–ReO₂ buffer assemblage and transport of rhenium under supercritical conditions. *Geochem. Transact.* 3, 1–10.
- Xiong, Y., Wood, S., Kruszewski, J., 2006. Hydrothermal transport and deposition of rhenium under subcritical conditions revisited. *Econ. Geol.* 101, 471–478.
- Xu, X.-W., Li, X.-H., Jiang, N., Li, Q.-L., Qu, X., Yang, Y.-H., Zhou, G., Dong, L.-H., 2015. Basement nature and origin of the Junggar terrane: new zircon U-Pb-Hf isotope evidence from Paleozoic rocks and their enclaves. *Gondwana Res.* 28 (1), 288–310.
- Xue, C., Chi, G., Zhao, X., Wu, G., Zhao, Z., Dong, L., 2016. Multiple and prolonged porphyry Cu–Au mineralization and alteration events in the Halasu deposit, Chinese Altai, Xinjiang, northwestern China. *Geosci. Front.* 7, 799–809.
- Yang, F., Chai, F., Zhang, Z., Geng, X., Li, Q., 2014. Zircon U-Pb geochronology, geochemistry, and Sr-Nd-Hf isotopes of granitoids in the Yulekenhalasu copper ore district, northern Junggar, China: petrogenesis and tectonic implications. *Lithos* 190–191, 85–103.
- Yang, F., Mao, J., Pirajno, F., Yan, S., Liu, G., Zhou, G., Zhang, Z., Liu, F., Geng, X., Guo, C., 2012. A review of the geological characteristics and geodynamic setting of Late Paleozoic porphyry copper deposits in the Junggar region, Xinjiang Uygur Autonomous Region, Northwest China. *J. Asian Earth Sci.* 49, 80–98.
- Yang, F., Yan, S., Qu, W., Zhou, G., Liu, F., Geng, X., Liu, G., Wang, X., 2010. The fluid inclusions and C, H and O isotopic geochemistry of the I mineralized zone at the Halasu copper deposit, Xinjiang. *Earth Sci. Front.* 17, 359–374 (in Chinese with English abstract).
- Zhang, F., Wang, Y., Liu, J., Wang, J., 2015. Zircon U-Pb and molybdenite Re–Os geochronology, Hf isotope analyses, and whole-rock geochemistry of the Donggebi Mo deposit, eastern Tianshan, Northwest China, and their geological significance. *Int. Geol. Rev.* 57 (4), 446–462.
- Zhang, Z., Mao, J., Cai, J., Kusky, T.M., Zhou, G., Yan, S., Zhao, L.i., 2008. Geochemistry of picrites and associated lavas of a Devonian island arc in the northern Junggar